CHALMERS UNIVERSITY OF TECHNOLOGY
Gothenburg, Sweden
www.chalmers.se

LICENTIATE THESIS

RUONAN LIU • Design and Application of High-speed Electrically Excited Synchronous Machines • 2026

Design and Application of High-speed Electrically Excited Synchronous Machines

RUONAN LIU

DEPARTMENT OF ELECTRICAL ENGINEERING
CHALMERS UNIVERSITY OF TECHNOLOGY
Gothenburg, Sweden 2026
www.chalmers.se

thesis for the degree of licentiate of engineering

Design and Application of High-speed Electrically Excited Synchronous Machines

Ruonan Liu

Department of Electrical Engineering
Chalmers University of Technology
Gothenburg, Sweden, 2026

Design and Application of High-speed Electrically Excited Synchronous Machines

Ruonan Liu

Acknowledgements, dedications, and similar personal statements in this thesis, reflect the author's own views.

Department of Electrical Engineering
Chalmers University of Technology
SE-412 96 Gothenburg, Sweden
Phone: +46 (0)31 772 1000

Printed by Chalmers Digital Printing
Gothenburg, Sweden, August 2026

Design and Application of High-speed Electrically Excited Synchronous Machines

Ruonan Liu
Department of Electrical Engineering
Chalmers University of Technology

Abstract

Electrically excited synchronous machines (EESMs) have emerged as a rare earth free alternative for EV (electric vehicle) traction, offering enhanced sustainability and operational flexibility. Furthermore, high-speed EESMs present a promising solution for achieving compact, efficient, and material-efficient traction systems, and have gained increasing attention in industrial applications.

First, An evaluation of high-speed EESMs based on the WLTC (Worldwide Harmonized Light Vehicles Test Cycle) driving cycle using a light EV model demonstrates that the operating points are distributed over a wide motor speed range. Across representative driving scenarios, including urban, countryside, and highway operation, these operating points are located within high-efficiency regions exceeding 96%, demonstrating that the proposed high-speed EESM consistently operates near its optimal performance. Furthermore, the selected light EV exhibits satisfactory dynamic capability, achieving a 0–100 km/h acceleration time of 8.1 s. This result confirms that the high-speed EESM provides a well-balanced performance, particularly under typical highway driving conditions.

Building upon this, the present study examines AC loss characteristics in a typical EESM equipped with hairpin windings. The results indicate that the solid losses are affected by the stator current angle, reaching a maximum near 45° and a minimum around 180°, with a difference of approximately 17.6% under identical current magnitudes. Furthermore, with a fixed stator current amplitude, increasing the rotor excitation current significantly elevates the AC resistance near 45°, while its effect remains limited near 180°. For the mechanical analysis of high-speed EESMs, both thermal expansion and centrifugal effects are considered. The results show that thermal expansion is the dominant factor influencing rotor stress and deformation, especially at elevated temperatures, while centrifugal force plays a secondary role even under high-speed conditions. Additionally, among the evaluated sleeve materials, carbon fiber provides the most effective structural reinforcement, producing the lowest stress and deformation.

This study presents the analysis of electromagnetic and structural design considerations in high-speed EESMs, providing a useful guidance for achieving improved performance, durability, and robustness in industrial applications.

Keywords Electrically excited Synchronous machine (EESM), electric machine design, AC losses, drive cycle, mechanical optimization.

To my family.

Contents

Acknowledgments

First and foremost, I would like to express my gratitude to my main supervisor Prof. Yujing Liu and my co-supervisor Dr. Luca Boscaglia, for their invaluable guidance, encouragement, and unwavering support. Their constructive feedback and insightful suggestions have played a crucial role in this research and have been essential to its completion.

I would also sincerely appreciate EU's Horizon Europe research and innovation program EU MSCA DN for the financial support, which has made this research possible.

Furthermore, I am grateful to my colleagues in the Department of Electrical Engineering at Chalmers University of Technology for providing a supportive research environment. The many enjoyable fika moments we have shared have made this journey both productive and memorable.

Finally, I would like to express my deepest appreciation to my parents and my friends for their unwavering love, encouragement, and support throughout my studies. Their understanding and belief in me have been a constant source of motivation.

Acronyms

EV:	Electric Vehicle
REE:	Rare Earth Elements
PMSM:	Permanent Magnet Sychronous Machine
IM:	Induction Machine
SynRM:	Synchronous Reluctance Machine
EESM:	Electrically Excited Synchronous Machine
NVH:	Noise, Vibration, and Harshness
WLTC:	Worldwide Harmonized Light Vehicles Test Cycle
FEM:	Finite Element Method

CHAPTER 1

Introduction

1.1 Background

Greenhouse gas (GHG) emissions have become a critical concern in the global effort to mitigate climate change, with fossil-fuel consumption remaining the primary source of CO_2. This dependence on fossil-based energy systems has accelerated global warming and increased the frequency of extreme climate events. Consequently, the change from fossil-based systems toward low-carbon technological solutions has emerged as an important requirement in international climate strategies.

As a major contributor to GHG emissions, the transportation sector has become a central focus in industrial and environmental policy discussions. According to the European Commission (EC), transport has represented the largest share of GHG emissions within the EU's Effort Sharing Regulation (ESR), accounting for 39% of total ESR emissions in 2024 [1]. Figure 1.1 illustrates the distribution of GHG emissions across ESR sectors from 2005 to 2030. As shown, total GHG emissions have exhibited a consistent declining trend since 2005. However,transport remains the largest contributor, indicating limited progress over the past 21 years. Therefore, To meet the

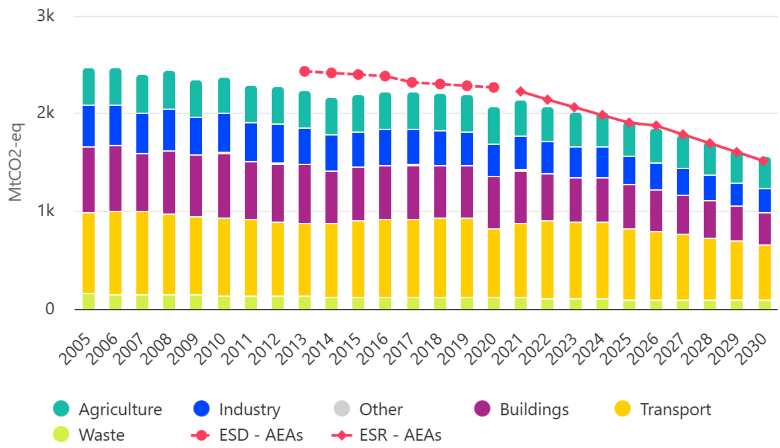

Figure 1.1: Emissions in sectors covered by effort sharing legislation 2005-2030 and annual emission allocations [1].

EU's climate objectives for 2030 and 2050, a substantial acceleration in the decarbonization of the transport sector is essential.

Road transport is the primary contributor to GHG emissions within the transportation sector. Between 2005 and 2023, emissions from road transport decreased by less than 5%, which indicates that the increase in zero-emission vehicles has been almost offset by the continued growth in road transport activity. To address this challenge, some key policies have been introduced, including gradually stricter emission standards for new passenger cars, vans, and heavy-duty vehicles.

Figure 1.2 illustrates the evolution of average CO_2 emissions from newly registered vans and the corresponding EU fleet-wide emission targets over the period from 2012 to 2035. Emissions show a gradual decline between 2012 and 2020, indicating the improvements in vehicle efficiency and emission reduction technologies. The figure also shows stepwise reductions in the EU fleet-wide emission limits, with substantial drops planned in 2025, 2030, and ultimately in 2035. As a result, all major road vehicle types are required to achieve zero emissions by 2035.

As an emerging alternative to conventional internal combustion engine vehicles, electric vehicles (EVs) represent a highly effective pathway toward achieving transport-sector decarbonization. In contrast to traditional fuel

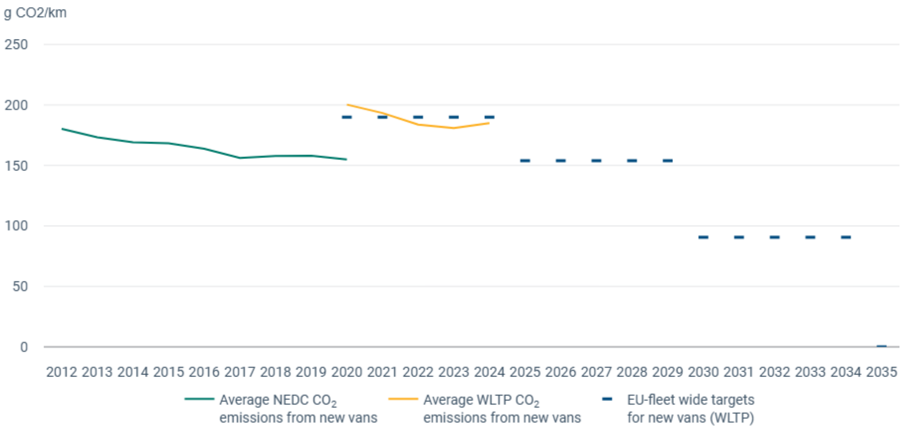

Figure 1.2: Trends in Average CO_2 Emissions from Newly Registered Vans and Corresponding EU Fleet-Wide Emission Targets (2012-2035) [2].

vehicles, EVs provide several notable advantages. They substantially reduce GHG emissions and contribute to improved urban air quality, especially when powered by low-carbon or renewable electricity sources. EVs enhance energy sustainability by enabling integration with renewable generation and supporting grid-flexibility services such as vehicle-to-grid (V2G) and smart charging. In operational terms, EVs are also characterized by quieter performance and lower maintenance requirements due to their reduced number of mechanical components. These combined benefits position EVs as a key technology for future sustainable transportation systems.

According to European Environment Agency (EEA), the registrations for EVs has increased to 23% in the total new vehicles registrations in 2023, which shows the demonstrates the accelerating market penetration of electrified transportation. Therefore,the need for EVs to achieve higher efficiency and enhanced performance has become increasingly prominent.

As a key component in EVs, traction motors play a crucial role in determining overall vehicle performance. Among the available technologies, permanent magnet synchronous machines (PMSMs) currently dominate the EV market due to the high efficiency, compact structure, and superior torque density. PMSMs rely extensively on rare earth elements (REEs) to achieve the required magnetic field. However, the environmental impact associated with REEs is substantial throughout the life cycle. The separation of REEs from ores requires intensive chemical processing, which can generate toxic tailings and heavy-metal residues causing pollution of surrounding soil and water systems. Moreover, recycling pathways for REEs remain limited and economically unattractive. According to the International Energy Agency (IEA), end-of-life recycling suffers from collection rates below 5% [3]. These challenges are further exacerbated by the uneven global distribution of REEs, which increases the risk of supply instability. In 2025, around 70% of global REEs are supplied by China, reflecting a highly concentrated supply chain [4].

To reduce the dependency on REEs, many other types of traction motors are explored as alternative options to PMSMs. Reluctance machines (RMs), by generating torque by aligning the rotor with the direction of lowest magnetic reluctance, is one of the approaches to replace PMSMs. Unlike PMSMs, reluctance motors do not require REEs. Main types of RMs include switched reluctance machines (SRMs) and synchronous reluctance machines (SynRMs). A typical design of RMs uses a wound stator and a laminated salient-pole rotor without magnets or rotor windings. Therefore, due to the structure, the key advantages of RMs are simple and robust construction, low manufacturing cost, independence from rare-earth resources, high thermal tolerance [5], [6], [7]. However, RMs suffer from significant torque ripple, which contributes to vibration and acoustic noise during operation. In addition, overall efficiency of RMs tends to become lower than PMSMs, particularly at low speeds and light load conditions. These limitations require more advanced control strategies and mechanical design to ensure competitive performance [8].

Induction machines (IMs) provide an alternative to avoid the use of REEs by generating torque through electromagnetic induction. With simple and robust construction, IMs provide high reliability in traction applications and maintain competitive performance under high thermal and mechanical loads [9]. IMs also offer low manufacturing cost, small torque ripple and low acoustic noise, which supports the adoption across a broad range of industrial applications [10]. Nevertheless, IMs require more complex control circuits, and both efficiency and power density are generally lower than those of PMSMs because part of the input energy becomes heat in the rotor. This limitation reduces overall performance, leading to a gradual decline in market share globally [11].

Electrically excited synchronous machines (EESMs) offer another REE-free alternative and are increasingly regarded as a more sustainable option for

EV traction applications. The excitation system of EESMs enables dynamic adjustment of the field current, providing direct control over the flux [12]. As a result, EESMs maintain good efficiency over a wide speed range and allow flexible magnetic field regulation, which enhances performance at high speeds. In addition, EESMs can deliver high power capability and maintain stable operation under demanding traction conditions [13]-[14].

Another approach to reduce material usage, particularly REEs, is to decrease motor size by increasing the operating speed. High speed operation reduces motor size since total power can be achieved with lower torque as rotational speed increases. At a fixed power level, the increase in operating speed reduces the required torque, which lowers the magnetic loading needed for torque and allows the rotor and stator dimensions to be reduced. In addition, higher operating speed enhances the frequency of electromagnetic energy conversion, which increases power density. Thus, it allows the same output power to be achieved with less material including copper and REEs. As a result high speed machines can be designed more compactly leading to reduced material usage particularly rare earth magnets while maintaining performance. With these advantages, high-speed machines have been increasingly used in industrial applications in recent years.

1.2 Electric Vehicles Requirements

In traction applications such as EVs, high-speed motors typically operate at rotational speeds significantly higher than conventional traction machines, often above 15000 rpm. Higher rotational speed contributes to enhanced power density, enabling the same output power to be delivered with a smaller amount of material and a more compact electromagnetic design. This trend improves the packaging of the electric traction system and allows tighter integration with other vehicle systems. At the same time, advances in inverter technology have enabled reliable operation at elevated electrical frequencies.

High-speed operation allows a traction motor to deliver the same mechanical power with a lower torque requirement, since output power is proportional to the product of torque and rotational speed. When the required torque decreases, the motor no longer needs a large electromagnetic air-gap radius or extensive volume to generate high torque. This directly reduces the stator and rotor dimensions, enabling a smaller electromagnetic structure without compromising the rated power. Smaller dimensions also reduce the size of supporting components such as the housing, bearings, and cooling structures.

These geometric reductions lead to lighter active components and more efficient utilization of magnetic and conductive materials. As a result, high-speed traction motors enable a meaningful reduction in machine mass, which can directly lower material-related costs. Reducing the mass of a traction motor contributes to improved vehicle efficiency and overall energy utilization. Lighter motors reduce the energy required for acceleration and decrease rolling resistance during driving.

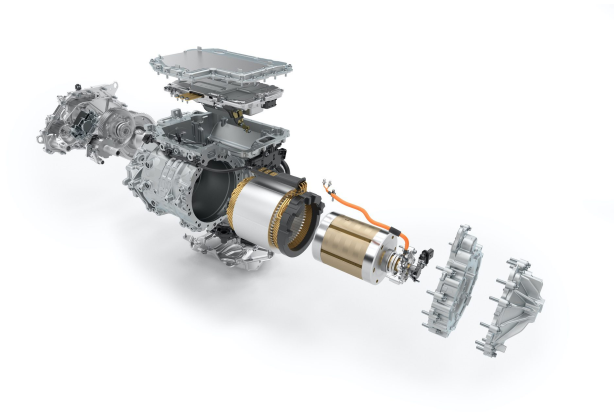

Figure 1.3: Exploded Illustration of the BMW iX Traction Motor and Integrated Electric Drive System.

With the benefits above, high-speed traction motors are increasingly adopted in modern electric drive systems. Several production vehicles already demonstrate this trend. Tesla Model 3 and Model Y, introduced in 2017 and 2019 respectively, employ interior permanent-magnet synchronous motors (IPMSMs) that operate at elevated speeds to achieve high torque density, compact packaging, and fast transient response. These drive units combine a high-speed rotor with advanced silicon-carbide (SiC) inverters, enabling efficient operation across a wide electrical-frequency range. BMW applies a similar approach in the iX, as illustrated in Figure 1.3. The BMW iX and the BMW i4, both introduced in 2021, use EESMs. In the iX, the EESM is designed for high-speed operation and integrated with the inverter and reduction gearing in a compact drive unit.

With the gear ratio corresponding to the maximum vehicle speed, the maximum motor rotational speed can be estimated. Accordingly, the maximum motor speeds for the high-speed traction machines introduced above are calculated as (1.1)(1.2) and summarized in Table 1.1.

$$n_{\text{wheel}} = \frac{v_{\text{vehicle}}}{2\pi R} \times 60 \tag{1.1}$$

$$n_{\text{motor}} = i_{\text{gear}} \cdot n_{\text{wheel}} \tag{1.2}$$

Table 1.1: Parameters of high-speed traction motors

EVs	Company	Maximum vehicle speed [km/h]	Gear ratio	Maximum motor speed [rpm]
Model 3	Tesla	225	9.03:1	18000
Model Y	Tesla	250	9:1	18500
iX	BMW	200	8.774:1	15000

Alongside Tesla and BMW, several other manufacturers have applied high-speed traction motors into EVs production. The Lucid Air utilizes a high-speed PMSM that reaches rotational speeds of up to 20,000 rpm, packaged in a compact drive unit to support high power density and long-range operation. Porsche uses high-speed IPMSMs in the Taycan, where elevated motor speeds contribute to rapid acceleration and enable the vehicle's two-speed rear gearbox architecture.

1.3 Previous Work

With the growing adoption of high-speed traction motors in modern electric-drive systems, improving motor performance has become increasingly important, requiring the achievement of key objectives such as lightweight design, high efficiency, enhanced thermal capability, and increased torque density.These targets drive research toward optimized electromagnetic design, loss reduction, and reliable operation under demanding conditions. Significant technical challenges associated with high-speed operation have emerged, motivating further investigation of the underlying electromagnetic, thermal, and mechanical phenomena.

To improve the torque, there are several studies about electromagnetic design optimization. Mistry *et al.* [15] proposed a holistic co-optimization framework for traction motor design that simultaneously satisfies electromagnetic, mechanical, and thermal requirements at rotor speeds exceeding 20,000 rpm. Allahyari *et al.* [16] introduces a multi-physics design methodology to enhance the performance of high-speed SynRMs by optimizing the design of the rotor flux guides. Iwaki *et al.* [17] presents a novel magnetic-geared motor consisting of a flux-modulated magnetic gear and a switched reluctance (SR) motor to achieve wide speed-torque characteristic. Ahn *et al.* [18] proposes a design process based on a multi-objective optimization algorithm, aiming to reduce the design cost of an axial flux permanent magnet motor for urban air mobility traction. One effective approach to improving machine performance is the use of hairpin windings, which have become widely adopted in traction motors. Compared with round wire windings, hairpin windings offer the following advantages[19]:

- Low DC resistance due to lager cross-section.
- High slot filling factor and high-torque density.
- Shorter end windings reducing cost and copper loss.
- Manufacturing process steps can be controlled easily.

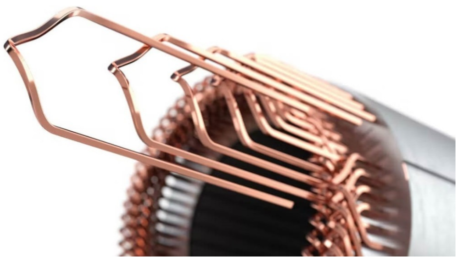

Figure 1.4: Hairpin winding

However, due to the large cross-sectional area, the AC losses of the hairpins are significant. Extensive studies have focused on accurately computing losses and developing methods to minimize the losses [20]-[21]. The effect of different layer numbers and aspect ratios on the AC loss of the hairpin is investigated using FEM [22]. In addition to the number of layers, [23] analyses the effect of slot size and slot height on hairpin AC loss. In [24], an equivalent model of AC loss considering conductor gap for hairpin and round conductor windings is proposed and validated by FEM.

For traction motors, thermal and mechanical analysis is also essential to ensure reliable performance in practical applications. High current loading and rapid torque transients generate significant heat, highlighting the need for accurate thermal modeling to assess temperature evolution and insulation constraints[25]. Mechanical analysis is also critical, as centrifugal forces, and vibration at high speed impose significant demands on rotor strength and structural stability. To address these challenges, many research has been conducted on accurate modeling and efficient solutions. By proposing a fast and accurate coupled electromagnetic–thermal analysis method, [26] integrates FEA-based parameter extraction with LUTs and an efficient thermal network model to enable iterative motor performance prediction over driving cycles with temperature-dependent effects. [27] built a multiphysics-based design framework for high-speed outer rotor motors, incorporating C-fiber reinforcement and optimized support configurations to address mechanical stress and vibration in integrated high-speed applications.

1.4 Contributions

With the increasing challenges related to electromagnetic losses and mechanical stresses in traction machines, the need for effective analysis and design solutions becomes essential. These challenges become even more severe under high-speed operation, as the impacts becomes more evident with increasing rotational speed. The purpose of this thesis is to address these issues for high-speed traction machines, especially for EESMs.

The main contributions are the following:

- The effect of the rotor magnetic field generated by the field current, stator current and the stator current angle on AC losses in a high-speed EESM is investigated. These factors directly affect the air gap flux distribution and the associated flux leakage, which become more pronounced at high speed. The correlation between saturation of stator core and AC losses is analyzed, as the saturation level alters the flux lines passing through the conductors and contributes to additional AC losses.

- The performance of high-speed EESMs under varying driving conditions has been evaluated using the driving cycle.The results demonstrate that EESMs achieve high efficiency, particularly under high-speed operating conditions, highlighting the suitability for such applications. Furthermore, the analysis shows that EESMs can still satisfy the performance requirements of typical passenger vehicles while offering improved efficiency and operating characteristics during highway driving conditions.
- The contributions of thermal expansion and centrifugal force to the maximum rotor stress and deformation in high-speed EESMs are analyzed separately, showing that thermal expansion has a stronger influence than centrifugal force, particularly at high temperatures. A sleeve is applied to the rotor surface to reduce stress and deformation, and its effectiveness is evaluated. A comparison of different sleeve materials, sleeve thicknesses, and operating conditions is performed. From the analysis of results, this thesis indicates that carbon fiber sleeve can provide an effective protection for high-speed traction EESMs.

1.5 Thesis Outline

With the aims above, the thesis begins with an introduction to the background and objectives of the study.

Chapter 2, provides the fundamental theories of electrical machines, including the model of electromagnetic losses, thermal and mechanical behaviors.

Chapter 3, presents the comparison between EESM and PMSM under varied vehicle driving conditions. The performance, including total efficiency and energy consumption, is evaluated by analyzing the efficiency map together with the corresponding operating points. By evaluating the 0–100 km/h acceleration time, the performance of the high-speed EESM is confirmed to be well suited for light EV applications.

Chapter 4, the influence of field current, stator current, and stator-current angle on AC losses in hairpin windings is analyzed using a high-speed EESM model with a rated speed of 18000 rpm. By evaluating the motor under different operating conditions, the AC resistance of the hairpin conductors is calculated. The effect of field current and current angle on AC resistance is verified by comparing the difference between AC resistance and DC resistance for different current angles.

Chapter 6, investigates the stress and deformation distribution in the rotor using a high-speed EESM model, assuming a maximum speed of 25000 rpm and a maximum operating temperature of 180 °C. The contributions of thermal expansion and centrifugal force to the peak rotor stress and deformation are evaluated under different operating conditions. The chapter also includes a comparative analysis of rotors with various sleeve materials, sleeve thicknesses, and application scenarios to assess the impact on mechanical protection at high speed.

1.6 List of Publications

[1] **R. Liu**, L. Boscaglia, B. Jiang and Y. Liu, "Impacts of Rotor Sleeves on Stress Distribution and Deformation in Electrically Excited Synchronous Machines," In *2026 International Conference on Electrical Machines (ICEM)*, Funchal, Madeira, Portugal, 2026.

[2] **R. Liu**, J. Tang, L. Boscaglia, B. Jiang, N. Sharma and Y. Liu, "Impacts of Stator Current Angle and Rotor Current on Solid Losses of Hairpin Windings in Traction Electrically Excited Synchronous Machines," In *2024 International Conference on Electrical Machines (ICEM)*, Torino, Italy, 2024.

[3] J. Tang, B. Jiang, L. Boscaglia, **R. Liu**, S. Lundberg and Y. Liu, "High-Frequency Brushless Excitation with Bi-Directional Power Flow for Electrically Excited Synchronous Machines," In *2024 International Conference on Electrical Machines (ICEM)*, Torino, Italy, 2024.

CHAPTER 2

Design of High-speed EESMs

With the continued evolution of traction motor research, increasing attention has been directed toward high-speed machine. High-speed operation introduces more demanding design constraints adn faster dynamic responses. Additionally, it also leads to more complex coupling among physical fields, establishing it as a significant and specialized area of study. As a result, high-speed traction motor research evolves from established foundations, but requires more multiphysics evaluation.

2.1 Machine Model

The dynamic model of EESMs is commonly expressed in the synchronous dq reference frame. The stator voltage and rotor field equations are given by

$$\begin{bmatrix} u_\mathrm{d} \\ u_\mathrm{q} \\ u_\mathrm{f} \end{bmatrix} = \begin{bmatrix} R_\mathrm{s} & 0 & 0 \\ 0 & R_\mathrm{s} & 0 \\ 0 & 0 & R_\mathrm{f} \end{bmatrix} \begin{bmatrix} i_\mathrm{d} \\ i_\mathrm{q} \\ i_\mathrm{f} \end{bmatrix} + \begin{bmatrix} 0 & -\omega_r & 0 \\ \omega_r & 0 & 0 \\ 0 & 0 & 0 \end{bmatrix} \begin{bmatrix} \psi_\mathrm{d} \\ \psi_\mathrm{q} \\ \psi_\mathrm{f} \end{bmatrix} + \frac{d}{dt} \begin{bmatrix} \psi_\mathrm{d} \\ \psi_\mathrm{q} \\ \psi_\mathrm{f} \end{bmatrix} \tag{2.1}$$

where $u_\mathrm{d,q}$ and u_f denote the stator and field voltages, $i_\mathrm{d,q}$ and i_f are the stator and field currents, and $\psi_\mathrm{d,q}$ and ψ_f represent the corresponding flux linkages. R_s and R_f are the stator and field resistances, respectively, and ω_r is the electrical angular speed. The flux linkages are expressed as

$$\begin{bmatrix} \psi_\mathrm{d} \\ \psi_\mathrm{q} \\ \psi_\mathrm{f} \end{bmatrix} = \begin{bmatrix} L_\mathrm{d} & 0 & L_\mathrm{m} \\ 0 & L_\mathrm{q} & 0 \\ \frac{3}{2}L_\mathrm{m} & 0 & L_\mathrm{f} \end{bmatrix} \begin{bmatrix} i_\mathrm{d} \\ i_\mathrm{q} \\ i_\mathrm{f} \end{bmatrix} \tag{2.2}$$

where L_d and L_q are the stator inductance in the d- and q-axis, L_f is the field winding inductance, and L_m is the mutual inductance between the stator d-axis and the field winding.

The inductance are considered as constant. Thus, the stator voltage equations together with the rotor field equation can be expressed as

$$\begin{bmatrix} u_\mathrm{d} \\ u_\mathrm{q} \\ u_\mathrm{f} \end{bmatrix} = \begin{bmatrix} R_s & -\omega_r L_\mathrm{q} & 0 \\ \omega_r L_\mathrm{d} & R_s & \omega_r L_m \\ 0 & 0 & R_\mathrm{f} \end{bmatrix} \begin{bmatrix} i_\mathrm{d} \\ i_\mathrm{q} \\ i_\mathrm{f} \end{bmatrix} + \begin{bmatrix} L_\mathrm{d} & 0 & L_\mathrm{m} \\ 0 & L_\mathrm{q} & 0 \\ \frac{3}{2}L_\mathrm{m} & 0 & L_\mathrm{f} \end{bmatrix} \frac{d}{dt} \begin{bmatrix} i_\mathrm{d} \\ i_\mathrm{q} \\ i_\mathrm{f} \end{bmatrix} \tag{2.3}$$

Under steady-state conditions, the derivatives of the currents are zero, i.e., $\frac{di}{dt} = 0$. The voltage equations therefore change to

$$\begin{bmatrix} U_\mathrm{d} \\ U_\mathrm{q} \\ U_\mathrm{f} \end{bmatrix} = \begin{bmatrix} R_s & -\omega_r L_q & 0 \\ \omega_r L_d & R_s & \omega_r L_m \\ 0 & 0 & R_f \end{bmatrix} \begin{bmatrix} I_\mathrm{d} \\ I_\mathrm{q} \\ I_\mathrm{f} \end{bmatrix} \tag{2.4}$$

Based on the representation in the d-q frame, the electrical power can be expressed as

$$P = \frac{3}{2}\left(u_\mathrm{d} i_\mathrm{d} + u_\mathrm{q} i_\mathrm{q}\right) \tag{2.5}$$

The electromagnetic torque can be expressed as

$$T_\mathrm{em} = \frac{3}{2} p \left[L_m i_\mathrm{f} + (L_d - L_q) i_\mathrm{d}\right] i_\mathrm{q} \tag{2.6}$$

2.2 Electromagnetic Losses Model

Electromagnetic losses in high-speed traction machines are mainly composed of copper losses in the windings and iron losses in the stator and rotor core. The fundamental copper loss in winding is expressed as

$$P_\mathrm{Cu} = \frac{3}{2} R_s (i_d^2 + i_q^2) \tag{2.7}$$

where R_s is the resistance of stator winding, i_d and i_q are stator currents in d-axis and q-axis respectively. For EESMs, the copper losses contain losses of rotor windings, which mainly can be calculated as

$$P_{Cu,r} = R_r \cdot i_f^2 \tag{2.8}$$

where R_r is rotor resistance, and i_f is field current. Temperature also affects the winding resistance, which can be expressed as

$$R = R_0\left[1 + \alpha(T - T_0)\right] \tag{2.9}$$

where α is the temperature coefficient of copper, and T is temperature of conductor. In high-speed traction motors, copper loss becomes more significant. As speed increasing, higher iron loss in stator core generate additional heat, which raises the winding temperature.

For hairpin windings, the effect of AC losses becomes more significant because of eddy current. When alternating current flows through a conductor, the varying magnetic field induces circulating currents inside the conductor. These eddy current cause the uneven current distribution in conductors, and thus increase AC losses. This phenomena is skin effect. Skin depth describes how deeply alternating current penetrates into a conductor, which can be formulated as

$$\delta = \frac{1}{\sqrt{\pi f \mu_0 \mu_r \sigma}} \tag{2.10}$$

where f is electrical frequency, σ is electrical conductivity of conductor material, and mu_0 and μ_r are relative magnetic permeability of vacuum and conductor material. From (2.10), skin depth reduces with increasing frequency, which showing the skin effect have a more significant impact under high-speed operation condition. In addition, each conductor in the stator slot can also be influenced by the magnetic fields produced by nearby conductors, which is known as the proximity effect. When current in nearby conductors varies with time, the resulting leakage magnetic fields induce additional eddy currents inside the conductor. The losses in single conductor caused by eddy current can be described as

$$P_{\text{eddy}} = \frac{\pi d^4\,\omega^2 B^2}{128\,\rho_c} \tag{2.11}$$

where d is conductor diameter, and B is flux density. To simplified the analysis of AC resistance, the following expression is used:

$$R_{\mathrm{AC}} = k_{\mathrm{ac}}\, R_{\mathrm{DC}} \tag{2.12}$$

where $k_a c$ is AC resistance factor. Under high-speed operation, $k_a c$ can exceed 1, indicating that the AC resistance is substantially greater than the DC resistance. This elevated resistance leads to higher copper loss and lowers the motor efficiency.

Besides copper loss, iron loss is also a major component of the electromagnetic losses in electrical machines. It occurs within the stator and rotor magnetic cores under alternating magnetic fields. When the main flux density changes with time, the steel lamination releases energy through hysteresis loss and eddy current loss. The magnitude of these losses is determined by the flux density, operating frequency, and material characteristics such as lamination thickness and resistivity. Iron loss in motors is commonly described using the loss-separation model, which expresses the total core loss as the sum of three physically different components. The total iron loss P_{Fe} is evaluated as

$$P_{Fe} = k_h B^n f + k_e B^2 f^2 + k_{\mathrm{ex}} B^{1.5} f^{1.5} \tag{2.13}$$

where B is the peak magnetic flux density and f is the electrical frequency. The first term, $k_h B^n f$, represents the hysteresis loss, and the coefficient k_h depends on the magnetic material properties, while n is the Steinmetz exponent, typically between 1.6 and 2.2. $k_e B^2 f^2$ corresponds to the classical eddy-current loss, and the coefficient k_e is mainly determined by the electrical resistivity and lamination thickness of the core material. $k_{\mathrm{ex}} B^{1.5} f^{1.5}$ represents the excess (or anomalous) loss caused by dynamic domain-wall motion in the magnetic material, and the coefficient k_{ex} reflects additional high-frequency loss effects.

In high-speed motors, iron loss becomes higher as both electrical frequency and flux-change rate scale with mechanical speed. Faster field reversal leads to more hysteresis loss. Rapid flux variation also generates stronger circulating currents in the laminations,which increases eddy current loss.

2.3 Thermal Model

In high-speed motors, thermal problems arise because several loss components increase with rotational speed and create concentrated heat sources throughout the machine. As the rotational speed rises, significant heat is generated in the stator windings due to higher AC copper loss. In the stator and rotor cores, main heat comes from increased hysteresis and eddy current loss. In the rotor surface, the heat is mainly from air friction and windage effects.

The lumped-parameter thermal network (LPTN) is a widely used method for estimating temperature distribution in electrical machines. It captures the main heat transfer paths with low computational effort, which makes it suitable for traction motor analysis. In LPTN model, the motor is represented by several thermal nodes connected through thermal resistances and capacitances. Each node corresponds to a physical region. Heat sources are assigned based on calculated losses. Thermal resistances describe heat transfer by conduction and convection between nodes. Thermal capacitances represent the thermal mass of each region and allow transient temperature changes to be modeled. The temperature of each node can be calculated as follows

$$C_{\text{th}} \frac{dT}{dt} + \frac{T - T_{\text{amb}}}{R_{\text{th}}} = P_{\text{themal loss}} \tag{2.14}$$

where C_{th} is thermal capacitance of the node, T and T_{amb} are the temperature of this node and ambient, while R_{th} is thermal resistance to the next node, P_{loss} is total thermal loss entering the node. The main LPTN equation relies on several loss and heat transfer terms as

$$C_{\text{th}} = \rho c_p V \tag{2.15}$$

$$R_{\text{th}} = \frac{L}{kA} \tag{2.16}$$

$$P_{\text{thermal loss}} = P_{\text{Cu}} + P_{\text{Fe}} \tag{2.17}$$

where ρ represents the density of material, c_p is the specific heat capacity, V is the volume, L is the conduction path length, k is thermal conductivity, and A is the cross-section area for heat flow. Among them, total thermal losses mainly contains copper loss and iron loss, as shown in (2.17).

In high-speed PMSMs, increased heating can push the permanent magnets close to the thermal limits. As a result, remanence and magnetic strength decrease, which may lead to partial demagnetization under severe operating conditions. These effects are especially critical in EESMs, where the rotor contains field winding that introduces additional copper losses. Limited rotor cooling in EESMs causes the increasing field winding temperature, which constrains the allowable current, excitation voltage, and maximum speed.Heat management relies on optimized cooling paths and properly engineered thermal interfaces, which makes thermal evaluation an important part of high-speed EESMs.

2.4 Mechanical Model

With increasing rotational speed, high-speed traction machines face increasing mechanical challenges. As the rotor spins faster, centrifugal loading becomes severe and can deform laminations, shift permanent magnets, or introduce fatigue in the shaft. The simplified relationship between centrifugal force and rotational speed is shown as

$$F_c = m\frac{v^2}{r} \tag{2.18}$$

where F_c is the centrifugal force (in Newtons, N), m is the mass of the object (in kilograms, kg), v is the tangential speed of the object (in meters per second, m/s), and r is the radius of the circular path (in meters, m).

For each rotor element, centrifugal force can be derivated as

$$dF = \rho\omega^2 r\, dV \tag{2.19}$$

where ω is angular speed (in radians per second, rad/s), r is the radial distance from the element to shaft center (in meters, m), dV repersents the volume of element (in cubic meter, m^3). For solid rotors, such as PMSM rotors, the rotor model can be simplified as a cylinder. The stress of the rotating cylinder in tangential and radial direction are represented as

$$\sigma_t(r) = \frac{3+\nu}{8}\,\rho\omega^2\left(R^2 - r^2\right) \tag{2.20}$$

$$\sigma_r(r) = \frac{3+\nu}{8}\,\rho\omega^2\,(R^2 - 3r^2) \tag{2.21}$$

where ν is the Poisson's ratio, R is the outer radius of rotor. According to (2.20) and (2.21), the centrifugal force on rotor rise with the square of rotational speed. At high speed, centrifugal forces generate significant mechanical loading on the rotor, increasing the risk of failure. This elevated stress can cause deformation in the rotor laminations.

In PMSMs, the permanent magnets can detach or shift if the retaining structure is insufficient. With windings in rotor, EESMs can provide control over the field flux. However, these copper windings can cause many mechanical challenges. One of them is the rotor stress due to the combination of centrifugal force and thermal expansion. When the rotor rotating in high speed, the windings and insulation materials experience significant centrifugal force that causing them to move outward. As the field current in the winding, Joule heating causes the copper wires expand more over than other surround materials which increases mechanical stress and strain at the interface between windings and laminations. This mechanical problem can increase the possibilities of insulation breakdown and mechanical fatigue over time. Therefore, the mechanical structure need to be considered during the design of high-speed EESMs.

Noise, vibration, and harshness (NVH) behavior also becomes an important mechanical challenge for traction motors operated at high speed. In traction applications, NVH analysis examines how these forces excite the stator, rotor, housing, and surrounding vehicle structures, ultimately influencing sound radiation and mechanical comfort. NVH in traction machines is driven by several mechanisms such as electromagnetic force harmonics, torque ripple, rotor imbalance, and structural resonances. These effects mainly come from electromagnetic forces, which can be decomposed into radial and tangential components respectively as

$$p_r(\theta, t) = \frac{B^2(\theta, t)}{2\mu_0} \tag{2.22}$$

$$p_t(\theta, t) = \frac{B_r(\theta, t)\, B_t(\theta, t)}{\mu_0} \tag{2.23}$$

where p_r and p_t are the radial and tangential force density, B is the air-gap magnetic flux density, B_r and B_t are the radial and tangential component of the flux, and μ_0 is the permeability of free space.

Radial force acts outward from the air gap surface and applies pressure to the stator teeth. Variations in radial force create strong radial vibrations that excite deformation and housing resonance. As a result, radial force is the main contributor to airborne noise in traction motors and produces many of the distinct noise components present during operation. The impact of radial electromagnetic force increases with the air-gap flux density. Tangential force is closely tied to torque production. When its magnitude varies, torque ripple is generated and excites vibration modes along the stator.

In NVH analysis, the rotor is constrained by the bearings and can move primarily in the radial direction. As a result, a single degree of freedom (SDOF) model is commonly used to represent the vibration behavior, which can be expressed as

$$m\ddot{x} + c\dot{x} + kx = F_{\text{em}}(t) \tag{2.24}$$

where m is the mass of the vibrating structure, c is the damping coefficient, k is the stiffness, x is the displacement, and $F_{\text{em}}(t)$ is the electromagnetic excitation force. In addition, the natural frequency of vibration mode from SDOF system can be represented as

$$f_n = \frac{1}{2\pi}\sqrt{\frac{k}{m}} \tag{2.25}$$

where f_n is the natural frequency and k is the structural stiffness. When the frequency of electromagnetic force harmonic matches the natural frequency (f_{EM}=f_n), resonance occurs and results in stronger vibration and noise.

At high operating speeds, NVH becomes more evident due to rapid variations in electromagnetic forces and higher electrical frequency. Increased centrifugal loading on the rotor adds to the resulting vibration and noise. High-speed operation also makes the system more sensitive to small geometric deviations, such as rotor imbalance, which can produce noticeable vibration and additional NVH components. Without the noise caused by combustion-engine, electromagnetic and mechanical noise from the motor in EVs becomes more noticeable.

CHAPTER 3

Performance Comparsion between EESM and PMSM

This chapter presents a comprehensive performance analysis and comparison between the high-speed EESM and PMSM. Motor performance is evaluated under multiple driving conditions, including highway, countryside, and city driving conditions, which represent the primary operating conditions experienced by electric vehicles in practical applications. Evaluating motor performance under these conditions enables a comprehensive assessment of operational effectiveness, facilitating a thorough evaluation of their suitability for practical EV applications.

The vehicle model in this chapter is first introduced, together with the key parameters of a typical light vehicle used throughout the subsequent analyses. The World Harmonized Light Vehicles Test Cycle (WLTC) is then presented to characterize the vehicle operating requirements under representative driving conditions. Based on these, the performance of the investigated EESM and PMSM are evaluated across different driving scenarios. By analyzing the efficiency under these operating conditions, it is demonstrated that the high-speed EESM offers a better performance in high-speed operating regions, making it particularly suited for highway driving applications.

3.1 Vehicle Model

The longitudinal vehicle model describes the forces acting on the vehicle along the direction of motion during a drive cycle. The traction force of vehicle and resistive force by road can be described respectively as

$$F_t = F_r + ma \tag{3.1}$$

$$F_r = F_{aero} + F_{grad} + F_{roll} \tag{3.2}$$

where F_t is the traction force, m is the vehicle mass, a is the vehicle acceleration, F_r is resistive force, F_{aero} is the aerodynamic force, F_{grade} is the gradient force, and F_{roll} is the rolling resistance force.

Aerodynamic drag increases with the square of vehicle speed and dominates traction demand at high velocities, making it particularly relevant for highway type drive cycles. The aerodynamic force is represented as

$$F_{aero} = \frac{1}{2}\rho C_d A v^2, \tag{3.3}$$

where ρ is the air density, C_d is the aerodynamic drag coefficient, A is the effective cross-sectional area of the vehicle, and v is the vehicle speed.

Gradient force occurs when the vehicle is driven on an incline or slope. The gradient force is represented as

$$F_{grad} = mg\sin(\theta), \tag{3.4}$$

where θ represents the road inclination angle, and g is the gravitational acceleration. Positive values of θ correspond to uphill driving, increasing traction demand, whereas negative values occur during downhill operation, enabling braking or regenerative energy recovery in electrified vehicles.

Rolling resistance represents the energy losses that occur when a vehicle's wheels roll over the road. Although rolling resistance is relatively small compared to aerodynamic force at high speeds, it becomes a dominant resistance force during low-speed urban driving, which is characteristic of many standard drive cycles. The rolling resistance force is represented as

$$F_{roll} = C_r F_n \tag{3.5}$$

where C_r is the rolling resistance coefficient, and F_n is the normal force acting on the wheels.

During driving, the total longitudinal force is translated into wheel torque and mechanical power.The traction torque and mechanical power of wheels can be described respectively as

$$T_w = F_t r_w \tag{3.6}$$

$$P_w = F_t v \tag{3.7}$$

where T_w is the wheel torque, r_w is the radius of the wheel, and P_w is the wheel power. The vehicle parameters selected for application analysis in this chapter are summarized in Table 3.1 [28]-[29].

From Table 3.1, the gear ratio has been set as 16:1. A higher gear ratio allows the traction motor to operate at higher speeds and lower torque levels for the given vehicle operating condition. For the high-speed EESM considered in this chapter, the elevated gear ratio also shifts the operating points toward the high-speed region, where higher efficiency can be achieved, particularly under highway driving conditions.

Table 3.1: Specifications of a typical light vehicle

Vehicle parameters	**Value**	**Unit**
Length	4694	mm
Width excluding mirrors	1933	mm
Height	1443	mm
Wheelbase length	2875	mm
Average track width	1580	mm
Wheel diameter	0.67	m
Curb weight	1609	kg
Top speed	150	km/h
Gear ratio	16:1	–
Aerodynamic drag coefficient	0.24	–
Effective cross section	2.23	m^2
Tire rolling resistance	0.012	–

3.2 WLTC Drive Cycle

Drive cycles are standardized speed–time profiles used in research and engineering. Such profiles enable consistent evaluation of vehicle performance, energy consumption, and emissions under controlled and reproducible conditions. Commonly used drive cycles differ in terms of geographical origin, driving characteristics, and intended application, thereby representing a wide range of operating conditions encountered in practice.

The Worldwide Harmonized Light Vehicles Test Cycle (WLTC) is a standardized drive cycle developed to provide a more representative assessment of vehicle performance compared to pervious drive cycles. By providing a broader range of speed profiles, including low, medium, high, and extra high-speed phases, the WLTC captures diverse driving dynamics. Enhanced acceleration and greater variability improve the representation of transient operating conditions. Such characteristics make the WLTC suitable for evaluating electrical vehicles under more demanding scenarios. Because of the improved representativeness and global harmonization, the WLTC has been widely adopted in recent automotive research and increasingly implemented in regulatory testing frameworks.

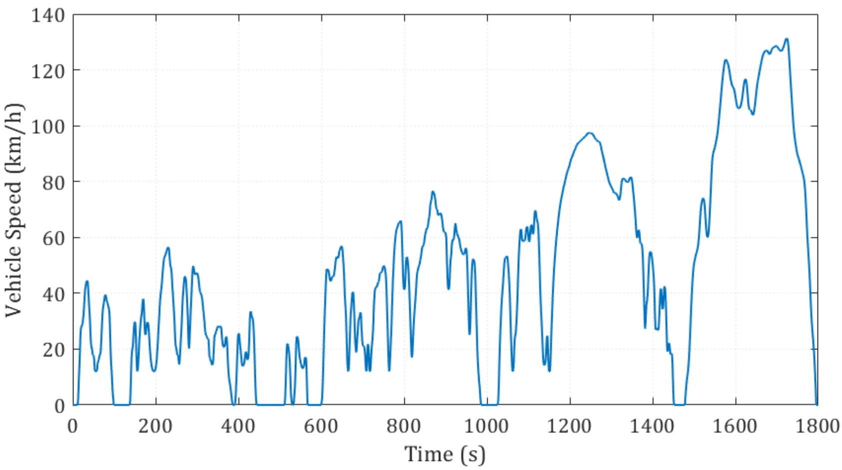

(a)

Figure 3.1: Vehicle and motor operating profiles corresponding to the WLTC driving cycle: (a) vehicle speed, (b) motor speed, and (c) motor torque.

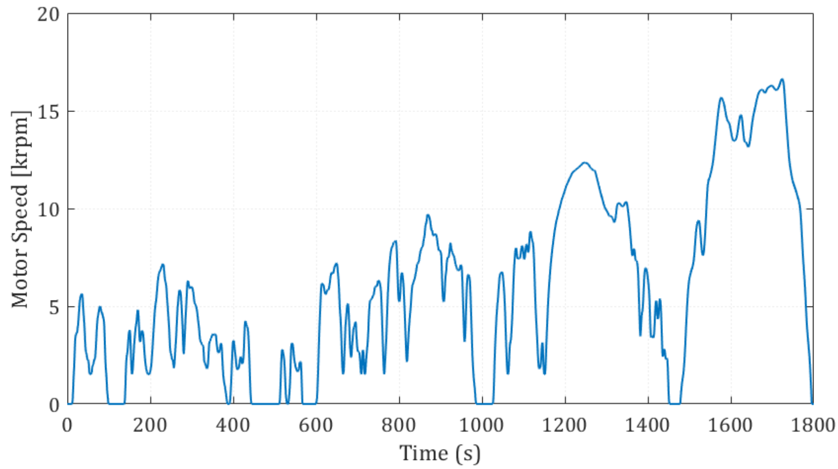

(b)

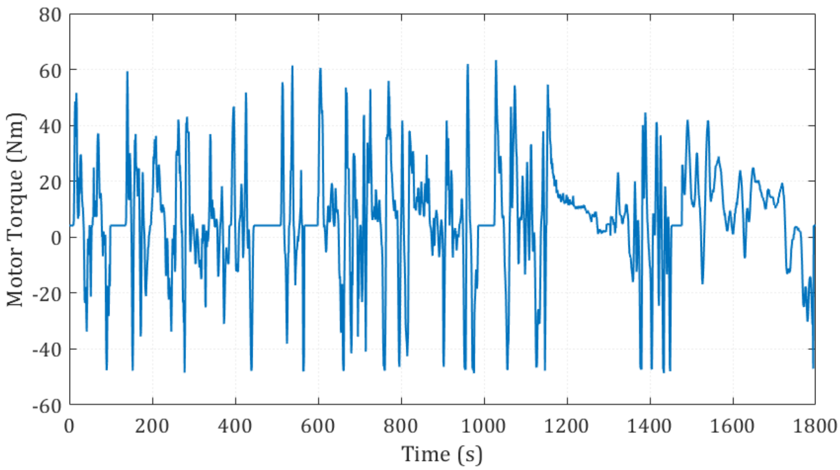

(c)

Figure 3.1: Vehicle and motor operating profiles corresponding to the WLTC driving cycle: (a) vehicle speed, (b) motor speed, and (c) motor torque.

Based on equation (3.1)-(3.7), the vehicle speed, motor speed and torque are shown in Figure 3.1. As shown in Figure 3.1(a), the WLTC consists of a combination of low-, medium-, high- and extra-high-speed conditions, representing a mixture of urban (0 - 589 s), countryside (590 s - 1022 s), and highway (1023 s - 1800 s) driving scenarios. With the vehicle speed profile shown in Figure 3.1(a), the higher gear ratio results in substantially increased motor speeds, as shown in Figure 3.1(b). Therefore, the motor operates over a wider high-speed range, reaching maximum approximately 16000 rpm during highway sections of the driving cycle. At the same time, the increased torque multiplication provided by the gear box as shown in Figure 3.1(c), allowing the required wheel torque to be achieved with a lower motor torque output.

3.3 Performance Analysis in Varied Driving Scenarios

This section presents a comprehensive performance comparison of the evaluated EESM and PMSM under representative electric vehicle driving conditions. Based on the vehicle model and the WLTC driving cycle, the operating points of both machines are analyzed together with their efficiency maps. The performance comparison focuses on the utilization of the operating region and the efficiency under highway, countryside, and city driving scenarios.

3.3.1 Evaluated EESM and PMSM Models

To facilitate a comprehensive comparison of the performance of the EESM and PMSM under various driving conditions, the 2D models of both machines were developed in ANSYS Electronics, as shown in Figure 3.2. The key design parameters of the evaluated motors are summarized in Table 3.2. To ensure a fair comparison, both machines share the same stator geometry and outer rotor diameter. In addition, the maximum operating speed of both machines is set to 18000 rpm, which is consistent with the requirements of high-speed EVs traction applications.

Table 3.2: Parameters of the evaluated EESM and PMSM model

Parameters	**Value**	**Unit**
Number of poles	8	–
Number of slots	48	–
Stator outer diameter	230	mm
Active length	158	mm
Peak power	100	kW
Peak torque	150	Nm
Peak operating speed	18000	rpm

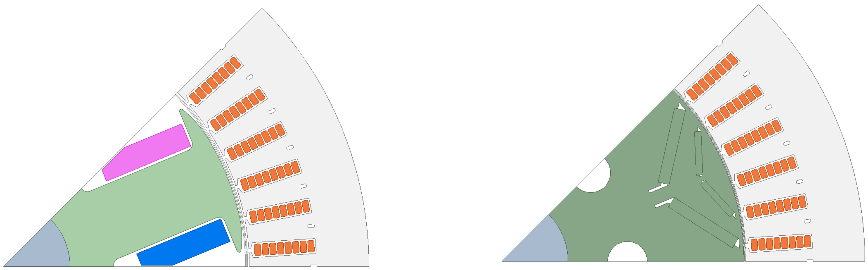

(a) **(b)**

Figure 3.2: One-eighth sector of the evaluated 2D motor model : (a) EESM, (b) PMSM.

3.3.2 Operating Points in Efficiency Maps

Based on the vehicle model and vehicle parameters, the efficiency map of the studied EESM and PMSM in this chapter with the operating points from WLTC is shown in Figure 3.3. From this figure, the operating points extracted from the WLTC cycle are distributed over a wide motor speed range, extending approximately from 0 up to 16500 rpm. As the motor speed increases, the operating points gradually concentrate in a narrower torque band and shift towards lower torque levels. This indicates that high-speed operation primarily corresponds to lower torque demand but higher rotational speeds, which is consistent with typical vehicle driving behavior under cruising conditions.

For EESM, a significant proportion of the operating points lie within the

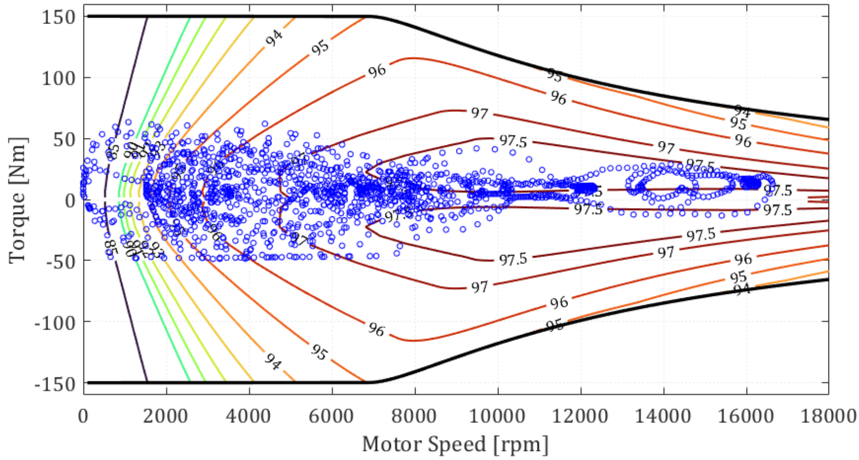

(a)

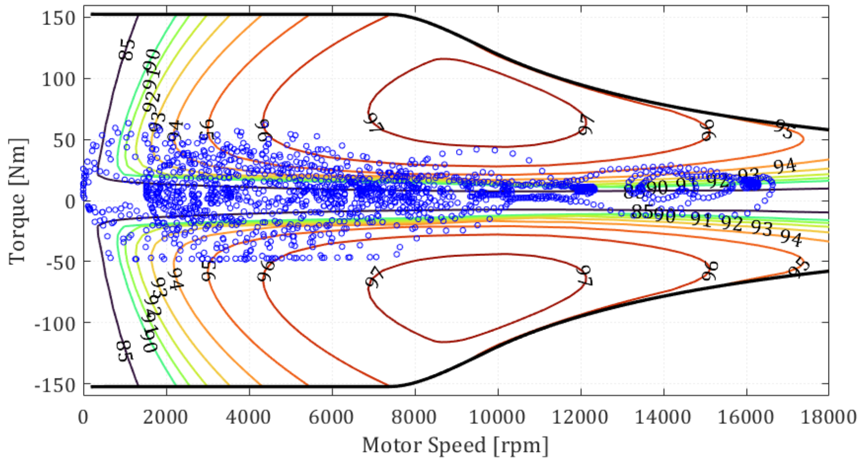

(b)

Figure 3.3: Efficiency maps (mechanical losses are not included) of the investigated high-speed motors with WLTC operating points distributions: (a) EESM and (b) PMSM.

high efficiency regions, approximately above 96–97%, as shown in Figure 3.3(a). This distribution demonstrates that the drive system, including the selected gear ratio, is effectively matched to the vehicle speed profile, ensuring that the motor operates close to its optimal efficiency region for most of the driving cycle. In contrast, the PMSM exhibits the high efficiency region primarily at medium speeds and higher torque levels, whereas many WLTC operating points are distributed outside these optimal regions, as shown in Figure 3.3(b). As a result, the EESM can operate more frequently at high-efficiency points throughout the driving cycle, leading to lower energy losses and higher overall drive-cycle efficiency. This demonstrates that the distribution of the efficiency map is as important as the peak efficiency itself when evaluating motor performance for practical EV applications.

3.3.3 Efficiency Comparison under Varied Driving Conditions

The efficiency map of the selected high-speed EESM and PMSM with several selected typical vehicle speeds under different driving scenarios is presented in Figure 3.4. As shown in this figure, the evaluated EESM consistently achieves higher efficiency than the PMSM across all the selected vehicle speeds. Table 3.3 presents the energy consumption of the EESM and PMSM over a complete WLTC cycle. For the WLTC distance of approximately 23.3 km, the EESM consumes 3.34 kWh, whereas the PMSM requires 4.10 kWh. This corresponds to an energy reduction of approximately 18.5% for the EESM. The lower energy consumption can be mainly due to the higher efficiency achieved by EESM in the high-speed operating region compared with PMSM. Consequently, the EESM experiences lower energy losses over the drive cycle, resulting in improved overall vehicle efficiency and driving range.

Table 3.3: Energy consumption in the WLTC cycle

Machine type	Energy consumption [kWh]
EESM	3.34
PMSM	4.10

The performance of evaluated EESM and PMSM with selected speeds including power and efficiency is shown in Figure 3.5 and Table 3.4. Among them, the representative operating points corresponding to common driving

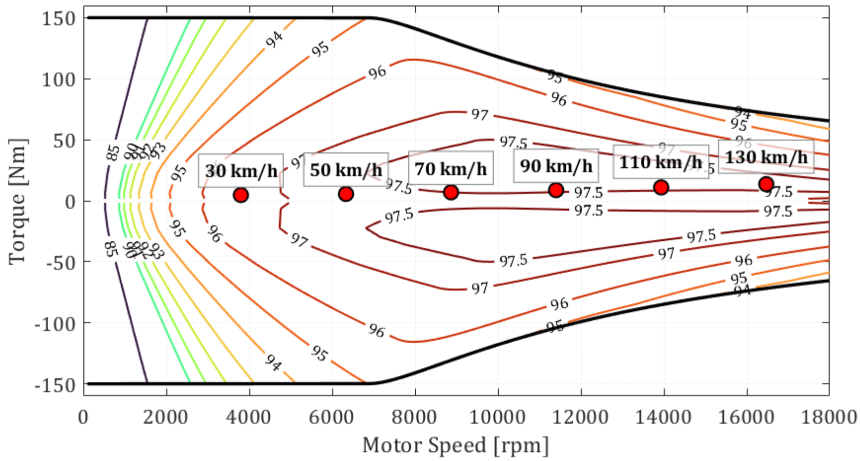

(a)

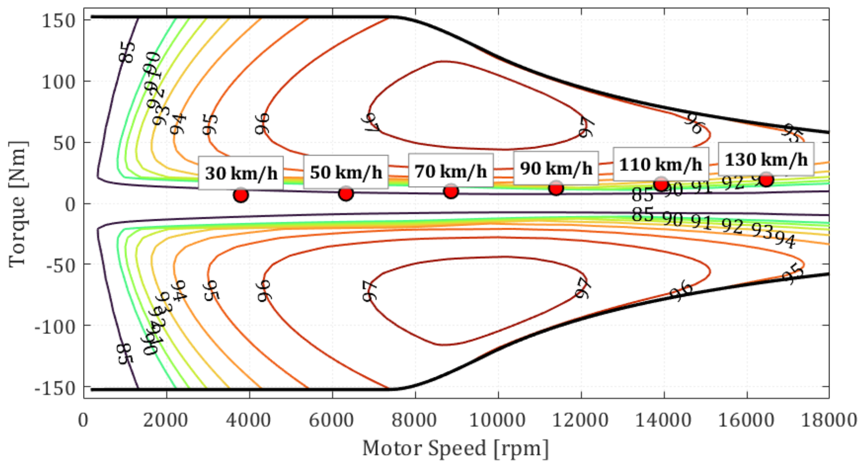

(b)

Figure 3.4: Efficiency map with varied vehicle speed in (a) EESM and (b) PMSM: 130 km/h, 110 km/h, 90 km/h as highway drive scenario; 70 km/h as countryside scenario; 50 km/h and 30 km/h as urban drive scenario.

conditions are highlighted. Highway operation is characterized by vehicle speeds of 130 km/h, 110 km/h, and 90 km/h, while 70 km/h is selected to represent countryside driving. For urban conditions, typical vehicle speeds of 50 km/h and 30 km/h are considered.

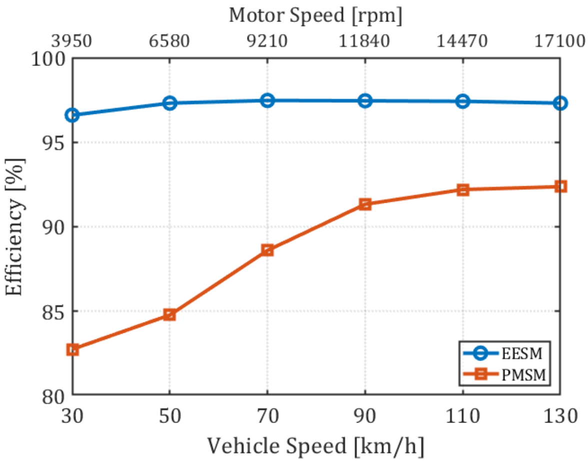

Figure 3.5: Efficiency comparison of EESM and PMSM with varied vehicle speeds.

Table 3.4: Performance comparison of EESM and PMSM under different driving scenarios

Driving condition	Speed [km/h]	Motor speed [rpm]	Torque [Nm]	Power [kW]	EESM [%]	PMSM [%]
Highway	130	17100	13.6	24.4	97.31	92.37
	110	14470	12.9	19.6	97.42	92.20
	90	11840	10.8	13.4	97.45	91.33
Countryside	70	9210	8.2	7.9	97.47	88.60
City	50	6580	5.8	4.0	97.31	84.78
	30	3950	3.9	1.6	96.60	82.75

Table 3.4 demonstrates that the high-speed EESM exhibits superior efficiency to the PMSM across all investigated driving conditions. At vehicle speeds of 90, 110, and 130 km/h, the EESM maintains efficiencies between 97.15% and 97.45%, whereas the PMSM achieves only 91.35% to 92.37%.

This advantage can be attributed to design emphasis of the EESM on high-speed operation, with the peak efficiency region closely matching the operating points associated with highway driving. As a result, the EESM achieves more effective utilization.

3.3.4 Acceleration Time Analysis

To further assess the performance of this vehicle, the acceleration time from 0 to 100 km/h is evaluated, as shown in Figure 3.6. The typical acceleration time for different EVs are presented in Table 3.5. From the result, the vehicle achieves 100 km/h in approximately 8.1 seconds.

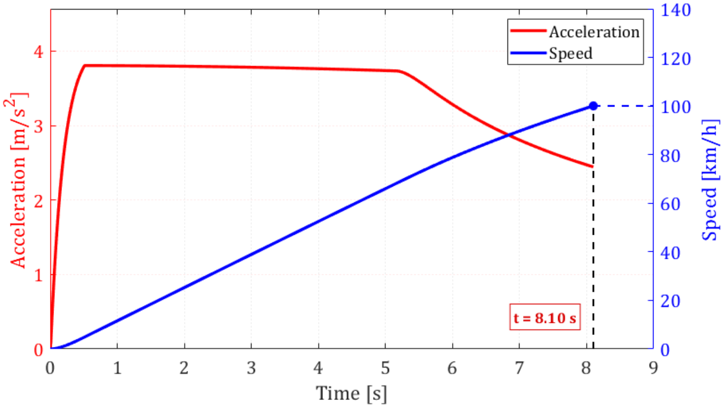

Figure 3.6: Acceleration and speed curve of the evaluated EV with EESM, showing a 0-100 km/h acceleration time of 8.10 s.

Table 3.5: Acceleration performance for different EV types

Vehicle category	Vehicle type	Acceleration (0–100 km/h)
Light EVs	Nissan Leaf	8.3 s
	Volvo EX30 P3 Long Range	8.3 s
	Evaluated EV	8.1 s
Mid-range EVs	Volvo EX90 Twin Motor	5.5 s
High-performance EVs	Tesla Model 3 Performance (Dual Motor)	3.3 s

As summarized in Table 3.5, representative light EVs such as the Nissan Leaf and Volvo EX30 exhibit similar acceleration times of around 8.3 s. Therefore, for a light EV, this level of acceleration can be considered good and well within the typical performance range expected for modern passenger vehicles.

3.4 Summary

This chapter analyzed the suitability of high-speed EESMs for traction applications by developing and analyzing a vehicle model. Based on the WLTC driving cycle, the resulting efficiency map demonstrated that the operating points are distributed over a wide motor speed range, covering nearly the entire operating region of the machine. Through the analysis of representative driving conditions, including highway, countryside, and urban operation, it is shown that the high-speed EESM can effectively address these operating points into regions of high efficiency. In particular, typical operating speeds corresponding to practical driving conditions are largely located within efficiency contours above 96–97%, indicating that the machine operates close to the optimal performance in most cases. When compared with the PMSM, the EESM exhibits a higher efficiency and lower energy consumption in the high-speed operating region, especially during highway driving.

In addition, the dynamic performance of the vehicle was evaluated, showing that a 0–100 km/h acceleration time of approximately 8.1 s is achieved. Compared with representative light electric vehicles, this level of performance is still competitive, indicating that high-speed EESMs are suited for light vehicle applications where efficiency, cost, and system optimization are prioritized.

CHAPTER 4

AC Losses in Hairpin Windings

For traction machines, the AC losses caused by magnetic leakage are significant in hairpin windings. The presence of adjustable field excitation in EESMs further increases the complexity of AC loss analysis. The aim of this chapter is to investigate the effect of the rotor magnetic field generated by the field current, stator current and the stator current angle on AC losses in EESM.

This chapter is based on the article:

- **R. Liu**, J. Tang, L. Boscaglia, B. Jiang, N. Sharma and Y. Liu, "Impacts of Stator Current Angle and Rotor Current on Solid Losses of Hairpin Windings in Traction Electrically Excited Synchronous Machines," *2024 International Conference on Electrical Machines (ICEM)*, Torino, Italy, 2024.

4.1 Effects of Current Angle and Field Current

The rotor magnetic field created by the field current and the stator magnetic field created by the stator current together form a synthetic magnetic field. This synthetic magnetic field passes through the stator core. The distribution of the flux in stator core will affect the distribution of flux leakage, which further influences the AC losses. The position of core saturation varies at different current angles, resulting in different amounts of AC losses.

In EESMs, the rotor field current is variable, causing it to affect the magnitude and location of the synthetic magnetic field. The stator current angle is the angle of the stator current to the d-axis, which also reflects the angle between the stator magnetic field and the rotor magnetic field. The magnetic field formed by the stator current is combined with the rotor field to form a flux linkage Φ. When this synthetic flux linkage of the d-axis and the q-axis points to a certain position in the stator, the core may be saturated at that position, as in Fig. 4.1. The additional flux in the form of leakage affects the hairpins in the neighboring slots, inducing eddy currents inside these hairpins and generating AC losses.

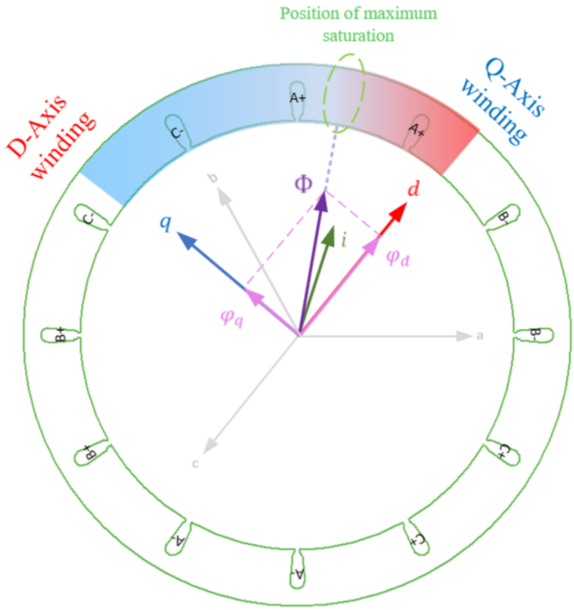

Figure 4.1: Schematic diagram of the current and magnetic chain in a typical motor model at a moment in time.

The different saturation positions are at various distances from the slots, causing eddy currents in the hairpins close to the slot openings, which ultimately show a correlation between the current angle and the AC losses. For example, Fig. 4.2 shows the magnetic circuit when there are 2 slots per pole per phase. From Fig. 4.2, the magnetic motive force (MMF) in stator yoke can be expressed as

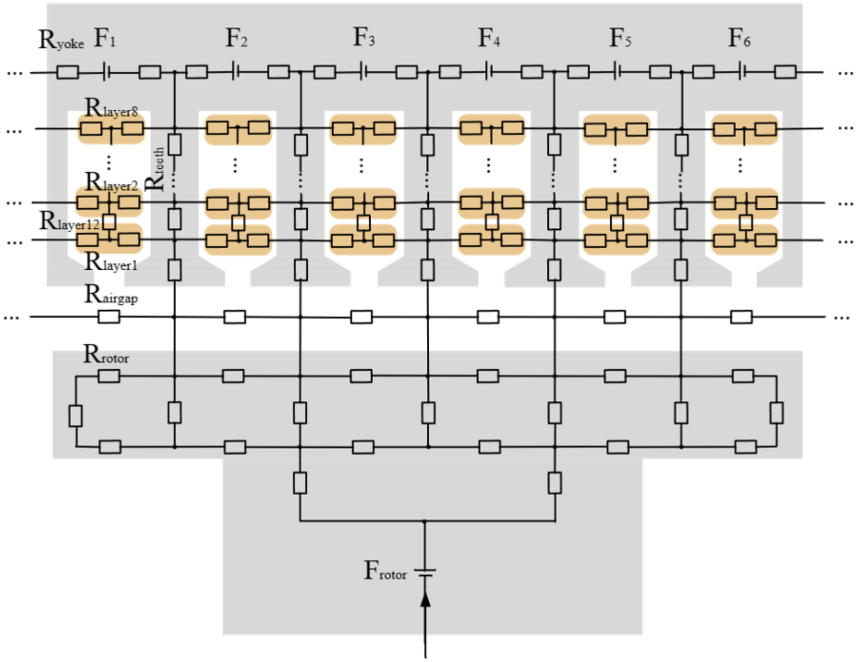

Figure 4.2: Equivalent magnetic circuit model of a single pole including stator, air-gap, rotor, and field flux paths.

The current flowing in each slot layer can be expressed as

$$F_i = \left| \frac{\sum_{n=1}^{N_{\text{layer}}} i_n}{N_{\text{parallel}}} \right| \tag{4.1}$$

where i_n is the current passing through the nth layer of the hairpin, N_{layer} is the number of layers in each slot, and N_{parallel} is the number of parallel paths. Since the three-phase currents passing through each slot are different, the MMF at the stator yoke corresponding to each slot can be expressed as

$$F_n = n_a i_a + n_b i_b + n_c i_c \tag{4.2}$$

where n_a, n_b, and n_c are the numbers of hairpins in one slot carrying the currents i_a, i_b, and i_c, respectively. And they conform to the following equation as:

$$\begin{cases} n_a n_b n_c = 0, \\ n_a + n_b + n_c = N_{\text{layer}}. \end{cases} \tag{4.3}$$

In (4.2), the three-phase currents i_a, i_b, and i_c can be written as

$$\begin{cases} i_a = I_d \cos(\omega t) - I_q \sin(\omega t), \\ i_b = I_d \cos\left(\omega t - \frac{2\pi}{3}\right) - I_q \sin\left(\omega t - \frac{2\pi}{3}\right), \\ i_c = I_d \cos\left(\omega t + \frac{2\pi}{3}\right) - I_q \sin\left(\omega t + \frac{2\pi}{3}\right). \end{cases} \tag{4.4}$$

The *d*–*q* can be expressed as:

$$\begin{cases} I_d = I_m \cos(\theta_i), \\ I_q = I_m \sin(\theta_i), \end{cases} \tag{4.5}$$

where I_m is the amplitude of the stator current and θ_i is the current angle. At current angles of 0°, 45° and 90°, the flux linkage of one pole is shown in Fig. 4.3.

When the current angle is 0°, the flux mainly passes through the stator teeth, and the reluctance in the magnetic circuit is small. When the current angle is 45°, the flux offset towards the q-axis, and a part of the flux goes through the hairpins in the slots. Being affected by current angle, the flux needs to flow in the tangential direction. The tangential reluctance in the air gap and the one in the stator slots are similar. Hence a significant portion of flux choose to flow in the slots, which induces eddy currents and AC losses. When the current angle is 90°, the flux goes through the stator teeth in the direction of the q-axis. At this time the flux going through the slots is affected by the current angle and passes through the hairpins in parallel. Since there is mainly the stator teeth reluctance and hairpins reluctance, the total reluctance in the magnetic circuit is less than at 45° and larger than at 0°.

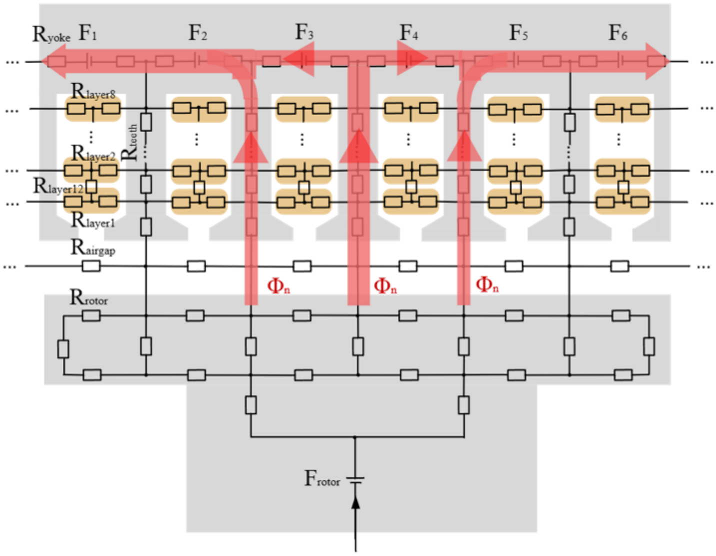

(a)

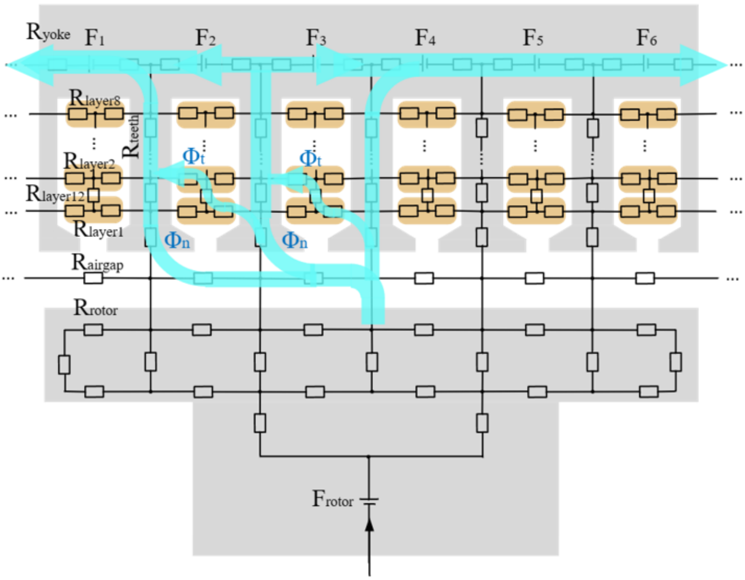

(b)

Figure 4.3: Flux paths in the equivalent magnetic circuit at different current angles: (a) 0°, (b) 45° and (c) 90°.

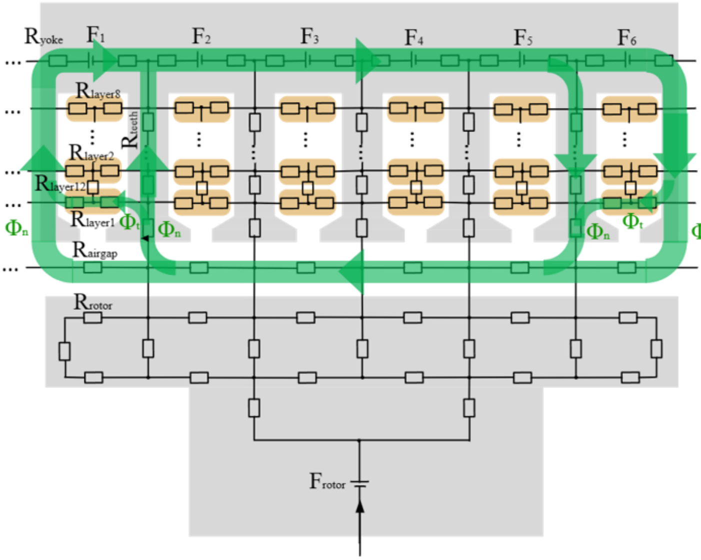

(c)

Figure 4.3: Flux paths in the equivalent magnetic circuit at different current angles: (a) 0°, (b) 45° and (c) 90°.

4.2 Simulation Model for AC Losses Analysis

To analyze the variation of AC losses with current angles and currents, a 2D model of EESM is established in ANSYS, as shown in Figure 4.4. The stator configuration is similar to that of conventional traction machines with hairpin windings. Each stator slot accommodates eight hairpin layers, and the cross-sectional geometry of the adopted hairpin conductor is presented in Fig. 4.5. The active part of DC resistance of hairpin is calculated as 3.1 mΩ. The main motor parameters are summarized in Table 4.1.

Since with each layers at different distances from the slot opening, the mesh size should not be the same for every hairpin. In order to get more accurate AC losses results, it is necessary to make the mesh size of the hairpin smaller than the skin depth. When the rotor rotating speed is 18000 rpm, the frequency is 1200 Hz. The calculated skin depth is 1.882 mm, as given by (2.10).

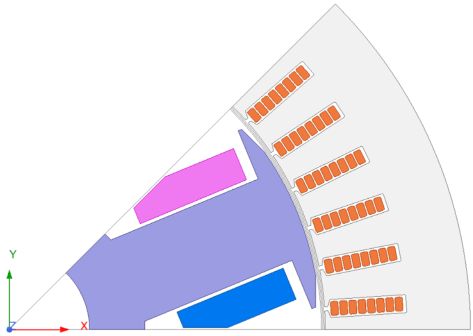

Figure 4.4: One-eighth sector of the 2D finite-element model of the investigated EESM.

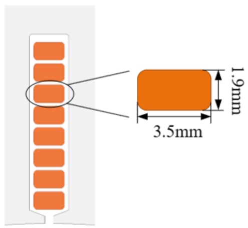

Figure 4.5: Cross-sectional layout of the eight-layer hairpin winding and dimensions of each conductors in the stator slot.

The closer the hairpin is to the slot the more slot harmonics it is exposed to and the less skin depth it has. Consequently, the upper layers of the winding experience more pronounced AC loss effects, particularly the first layer. For an 8-layer hairpin winding considered in this chapter, the first two layers are more affected to slot harmonics. Therefore, the mesh of the first two layers should not exceed 1.882 mm. Considering both computational accuracy and simulation efficiency, a non-uniform meshing strategy is adopted, with refined meshes applied to the upper layers and normal meshes used in the remaining conductors. The final hairpin mesh settings are summarized in Table 4.2, and the resulting finite-element mesh of the motor is illustrated in Fig. 4.6.

Table 4.1: Parameters of the evaluated EESM model

Parameters	**Value**	**Unit**
Number of poles	8	–
Number of slots	48	–
Stator outer diameter	230	mm
Airgap length	0.75	mm
Active length	148	mm
Operating peak stator current	600	A
Peak power	300	kW
Peak torque	460	Nm
Peak operating speed	18000	rpm

Table 4.2: Mesh size of each layer hairpin

Layers of hairpin	**Value**	**Unit**
1st–2nd layer	0.5	mm
3rd–8th layers	2	mm

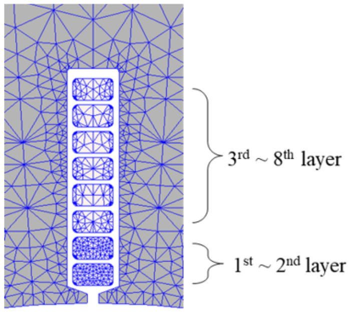

Figure 4.6: Mesh distribution of different hairpin layers in one slot.

4.3 Results of Current Angle and Field Current

Based on the motor model above, considering the current angle and field current as the two affecting factors, the AC losses of total and each layer of hairpin are analysed as follows. Since the AC losses at the same current but different speeds are identical in shape, only the AC losses at 6000 rpm are presented and compared in this section, which is the base speed of this motor.

4.3.1 Flux Lines Distribution Analysis

With the maximum stator current, the flux lines at 0°, 45° and 90° are shown in Figure 4.3 respectively, for different field currents. When field current is 0, the direction of the flux lines at different current angles is consistent with the analysis in Figure 4.3. When there is a field current, the flux in the d-axis direction is strengthened, causing the total flux to be shifted towards the d-axis direction, which is obvious in Figure 4.3 (b).

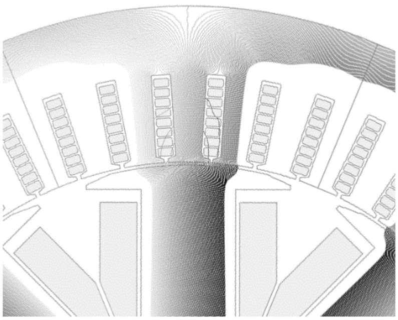

(a) 0 A

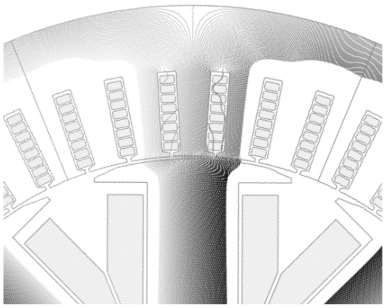

(b) 5 A

Figure 4.7: Flux lines at a current angle of 0° for different field currents: (a) 0 A, (b) 5 A.

From section 4.1, saturation of the stator is related to the total flux. In this motor, the total flux comes from stator current and field current. Figure 4.10 shows the AC losses when the stator and rotor currents apply separately. Since the AC losses when only field currents is applied are small and constant regardless of the current angle, as the results shown in Figure 4.10. It is shown in Figure 4.10 (a) that the AC losses are more current angle dependent when the stator current increases. This is due to the fact that, when the stator core is saturated, the core reluctance increases and then, the leakage flux increases.

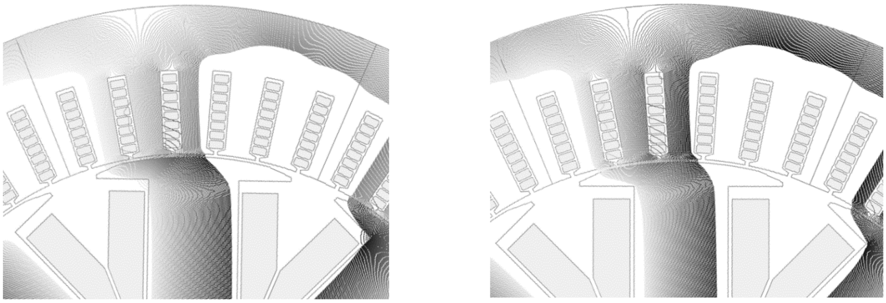

(a) 0 A　　(b) 5 A

Figure 4.8: Flux lines at a current angle of 45° for different field currents: (a) 0 A, (b) 5 A.

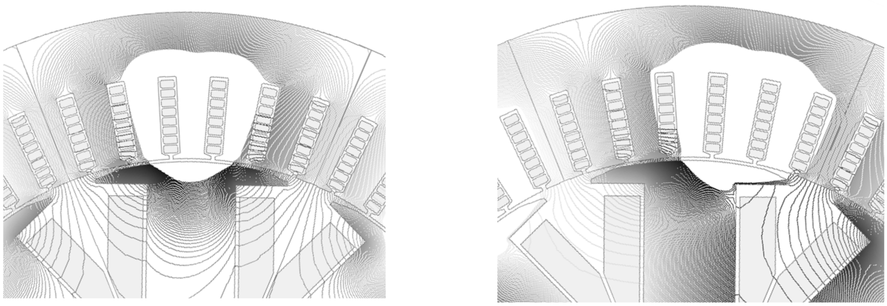

(a) 0 A　　(b) 5 A

Figure 4.9: Flux lines at a current angle of 90° for different field currents: (a) 0 A, (b) 5 A.

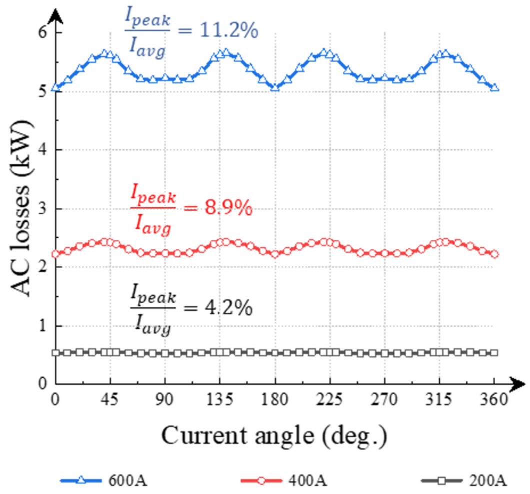

(a)

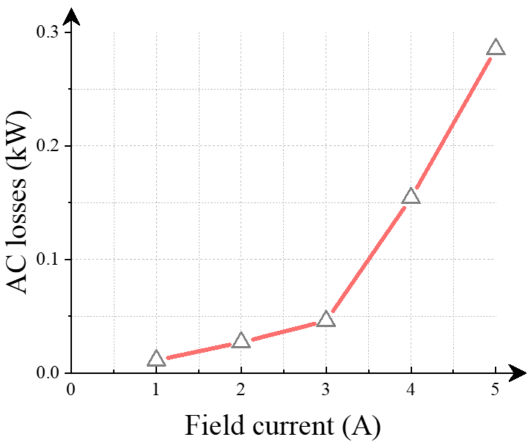

(b)

Figure 4.10: AC losses at 6000 rpm with (a) stator current variation and (b) field current variation respectively .

4.3.2 Effect on total AC losses

Figure 4.11 shows the AC losses when the stator current and field current operate simultaneously. From Figure 4.11 (a), when stator current is relatively small, AC losses reduces with field current at 180° compared to no field current. It is because the flux produced by field current at 180° in d-axis counteracts stator magnetic flux and eases core saturation. When stator current is 400 A in Figure 4.11 (b), AC losses show the similar tendency with Figure 4.11 (a) at 5 A field current. When field current is less than 5 A, AC losses are dependent on current angle. This is because the rotor flux produced by field current at 180° is not high enough to ease the core saturation. In Figure 4.11 (c), when the stator current is 600 A, the AC losses vary with current angle regardless of the existence of field current. This is because the core is deeply saturated at this stator current. And flux produced by field current of 5 A is too low to alleviate core saturation. Thus, the AC losses are dependent on current angle.

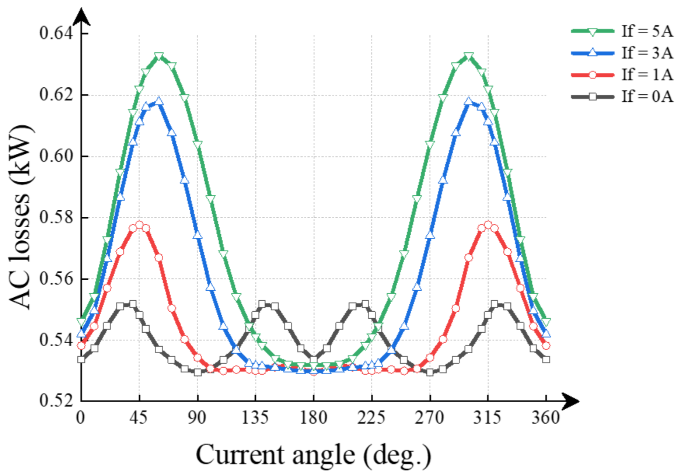

(a)

Figure 4.11: AC losses at different filed currents of 6000 rpm when stator current is (a) 200 A, (b) 400 A, and (c) 600 A.

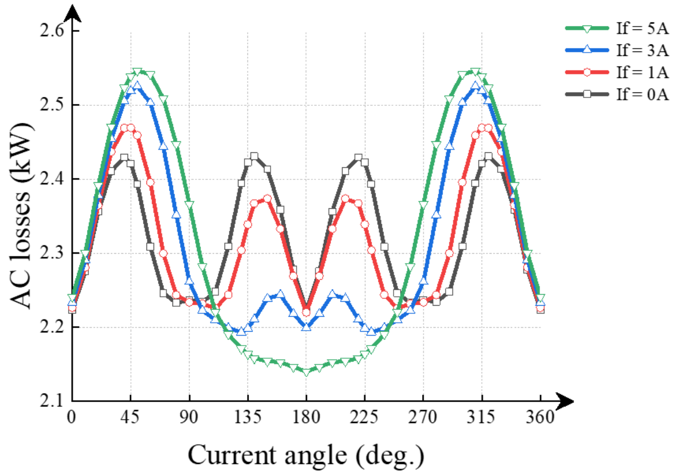

(b)

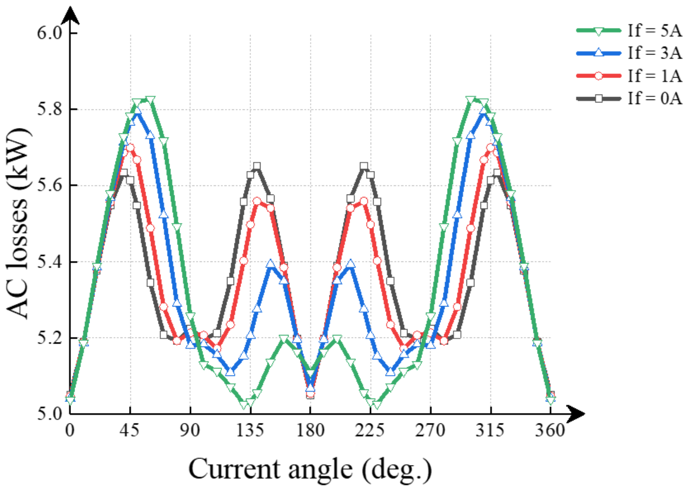

(c)

Figure 4.11: AC losses at different filed currents of 6000 rpm when stator current is (a) 200 A, (b) 400 A, and (c) 600 A.

Based on the AC losses results, AC resistance can be calculated as shown in Figure 4.12. From Figure 4.11 and Figure 4.12 , the AC losses and AC resistance reach maximum values close to the current angle of 45° and decrease as the angle approaches 180°, regardless of field current. Comparing the AC resistance with the DC resistance, as shown in Figure 4.13. As can be seen in Figure 4.13, the tendency of AC resistance is similar to AC losses at the same stator current.

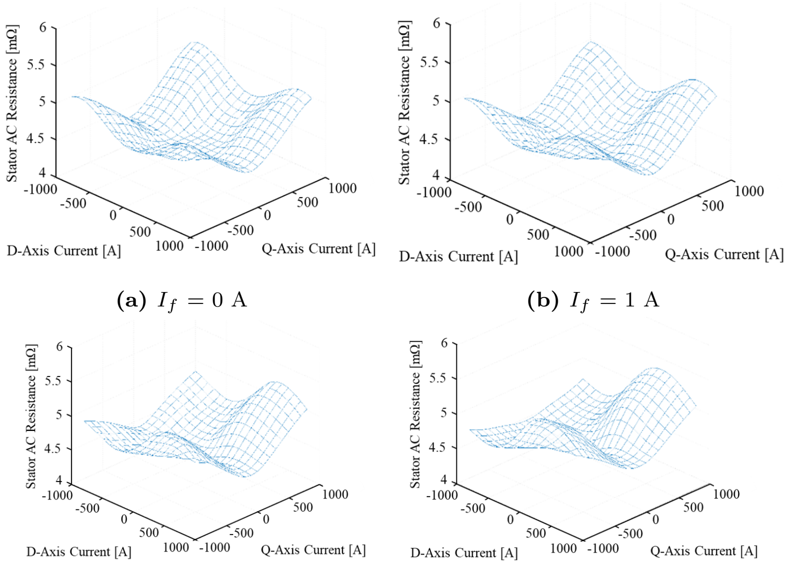

(a) $I_f = 0$ A (b) $I_f = 1$ A (c) $I_f = 3$ A (d) $I_f = 5$ A

Figure 4.12: AC resistance at different currents and current angles

Numerical analysis shows that, for a typical EESM used in this study, hairpin solid losses reach the maximum at around stator current angle 45° and the minimum at around 180°. The maximum is approximately 17.6% higher than the minimum at the same rotor current and stator current amplitude. When the rotor current increases with the stator current amplitude fixed, the hairpin AC resistance tends to increase significantly around 45°, but changes not much around 180°. When the stator current amplitude increases with the rotor current fixed, the but AC resistance reaches a maximum of 73% higher than the DC resistance.

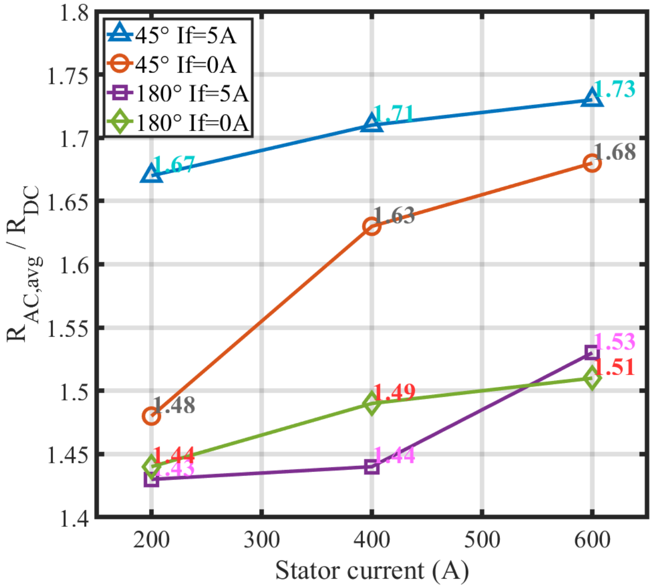

Figure 4.13: Comparison of AC resistance ratio ($R_{\mathrm{AC,avg}}/R_{\mathrm{DC}}$) with varied stator current at current angles of 45° and 180°, for field currents of 0 A and 5 A.

4.4 Summary

In this chapter, the impacts of stator current angle and rotor current on solid losses of hairpin windings in traction electrically excited synchronous machines have been analysed with assistance of FEM. The stator iron core saturates as the rotor current increases. This leads to higher leakage flux and therefore higher hairpin solid losses. The stator current introduces armature reaction which distorts the main flux distribution generated by rotor current, and the location of saturation moves.

CHAPTER 5

Mechanical Analysis Considering Speed and Temperature Effects

For high-speed EESMs, the field windings in the rotor slots can introduce deformation and stress to the rotor laminations, resulting in uneven airgap. This chapter aims to investigate the contributions of stress and deformation on rotor under different operating conditions. Furthermore, the role of sleeves as a protection is studied, to ensure safe and efficient motor operation at high-speed operating conditions.

This chapter is based on the article:

- **R. Liu**, L. Boscaglia, B. Jiang and Y. Liu, “Impacts of Rotor Sleeves on Stress Distribution and Deformation in Electrically Excited Synchronous Machines,” In *2026 International Conference on Electrical Machines (ICEM)*, Funchal, Madeira, Portugal, 2026.

5.1 Motor Structure

The EESM studied in this chapter has 8 poles and the excepted maximum speed is 25000 rpm and maximum operation temperature is 180 °C. The lamination material considered for the rotor is M250-35A and the main parameters are shown in Table 5.1. In this paper, the rotor stress and deformation with different sleeves is taken into account. There are three kind of materials used in the following analysis: Ti-6Al-4V, carbon fibre and Inconel 718. The physical properties of the sleeves materials are shown in Table 5.1.

Table 5.1: Parameters of Motor

Parameters	**Value**	**Unit**
Number of poles	8	–
Airgap length	1.5	mm
Outer diameter	132	mm
Active length	160	mm
Rotor slot filling factor	40	%
Rotor current	10	A
Peak power	300	kW
Continuous power	100	kW
Peak torque	460	Nm
Continuous torque	60	Nm
Peak operating speed	25000	rpm
Base speed	8000	rpm
Rotor Winding Insulation Class	180	°C

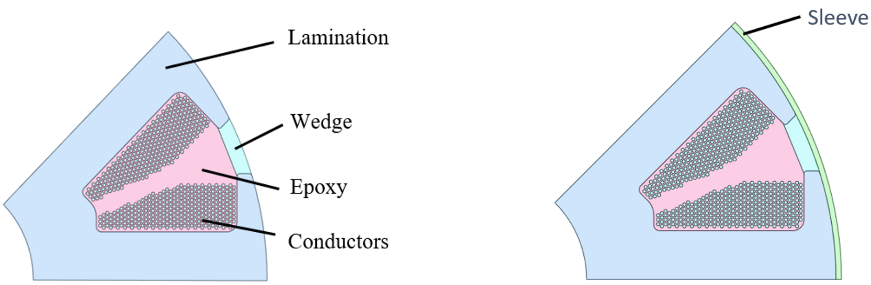

(a) Without sleeve. **(b)** With sleeve.

Figure 5.1: Cross section of different rotor structures: without sleeve and (b) with sleeve.

To reduce simulation time while preserving structural symmetry, a one-eighth segment of the rotor has been modeled, as shown in Figure 5.1. For enhanced accuracy, a 3D model of rotor was built with a lamination thickness of 0.35 mm, representing a single lamination sheet. A wedge is inserted between each pair of rotor poles to secure the windings and prevent displacement from the rotor slots. The number of conductors in each rotor slot is determined based on the filling factor. In addition to copper conductors, the windings are embedded in resin epoxy to maintain mechanical stability.

Table 5.2: Properties of Sleeve Materials

Properties	**Ti-6Al-4V**	**Carbon fiber**		**Inconel 718**
		Tangential	*Radial*	
Density [kg/m^3]	4429	1800	1800	8820
CTE [1/K]	8.79×10^{-6}	-1×10^{-6}	8×10^{-7}	1.3×10^{-5}
Young's modulus [GPa]	111	208	20	165
Poisson's ratio	0.34	0.4	0.2	0.3
Tensile strength [MPa]	845	1300	-67	1100

The cross-sectional view of the rotor model is shown in Figure 5.1 (a). Figure 5.1 (b) shows the cross section of the rotor model with sleeve. The sleeve provides additional structural reinforcement and is press-fitted onto the rotor lamination to enhance fixation, with a press-fit tolerance set to 0.02 mm. In addition, the contact type between lamination and wedge in the model is bonded, and between lamination and winding is frictional to better simulate the motion. Based on the operational speed and temperature ranges, the mechanical simulations are performed by varying the rotational speed from 0 to 25000 rpm and the temperature from 20 °C to 180 °C. The environment temperature is set as 20 °C.

5.2 Stress Analysis

In mechanical analysis with ANSYS, the *EquivalentStress*, also referred to as *vonMisesstress*, represents an equivalent uniaxial tensile stress that would produce the same level of distortion energy as the actual multiaxial stress state. *EquivalentStress* correlates well with the onset of yielding in ductile materials, which can be defined as

$$\sigma_{\text{eq}} = \sqrt{\frac{1}{2}\left[(\sigma_1 - \sigma_2)^2 + (\sigma_2 - \sigma_3)^2 + (\sigma_3 - \sigma_1)^2\right]} \tag{5.1}$$

where σ_1, σ_2, and σ_3, are the principal stresses. In this study, the maximum *Equivalent Stress* is used as the primary metric to evaluate the structural integrity of the rotor under different operational conditions.

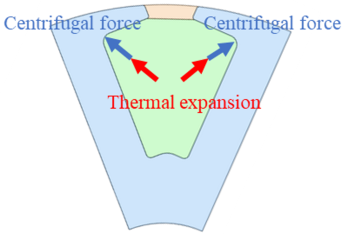

Figure 5.2: Diagram of the stress on pole shoe corner by thermal expansion and thermal expansion.

Figure 5.3 shows the stress distribution in different rotor structures at the worst case equal to 25000 rpm and 180 °C. From this figure, the position of maximum stress happens on the pole shoe corner in the rotor without sleeve, with Titanium alloy sleeve and Inconel 718 sleeve. For rotor with carbon fiber sleeve, the maximum stress happens on the sleeve from Figure 5.3 (c). Besides, there are stress on the all three kind of sleeves, which shows the effectiveness.

5.3 Deformation Analysis

At high-speed, the lamination gets deformed due to the centrifugal forces and thermal expansion. In this Section, an analytical model for rotor deformation is presented. Based on the 3D model developed in Section 5.1, rotor deformation was simulated using ANSYS Mechanical, and the resulting deformation distribution is illustrated in this section.

Since the most effect of thermal expansion is on the airgap, the following calculation focuses on the cylinder surface of rotor which is the outer edge of the model in Figure 5.1 For a hollow cylinder, the deformation caused by thermal expansion on the outer surface of rotor can be calculated as

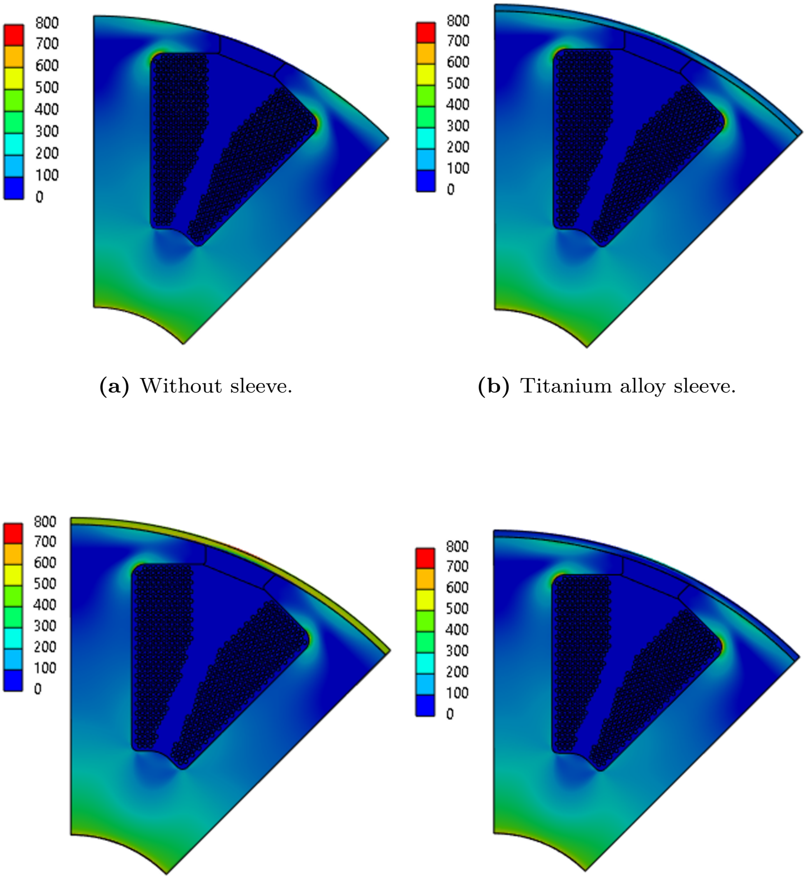

(a) Without sleeve.

(b) Titanium alloy sleeve.

(c) Carbon fiber sleeve.

(d) Inconel 718 sleeve.

Figure 5.3: Comparison of rotor mechanical stress distributions at 25000 rpm and 180 °C for different sleeve configurations: (a) without sleeve, (b) titanium alloy sleeve, (c) carbon-fiber sleeve, and (d) Inconel 718 sleeve.

$$\Delta r = \alpha r_0 \Delta T \tag{5.2}$$

where Δr is the radius expansion, α is the CTE of material, r_0 is the initial radius, and ΔT is the temperature change. For a more complicated model, the thermal expansion happening on the rotor can be calculated as

$$\mathbf{u}(r, \theta, z) = \alpha \cdot \Delta T(r, \theta, z) \cdot \mathbf{x} \tag{5.3}$$

where $\mathbf{u}$ is the thermal displacement vector and $\mathbf{x}$ is the position vector. From (5.3), each point in the model expands outward from its original position proportionally to the local temperature change. Fig. 5.4 shows the diagram of maximum deformation caused by centrifugal force and thermal expansion.

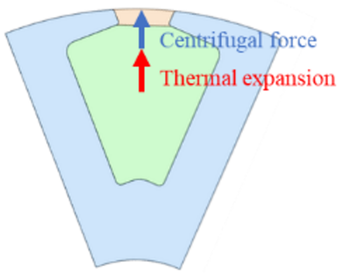

Figure 5.4: Diagram of the deformation on rotor slot by centrifugal force and thermal expansion.

In the structural analysis of ANSYS, the *Total Deformation* represents the magnitude of the overall displacement vector at each node of the structure, which is calculated as

$$U_{\text{total}} = \sqrt{u_x^2 + u_y^2 + u_z^2} \tag{5.4}$$

where u_x, u_y and u_z are the deformation on the x, y and z axes separately. u_x in cylinder coordination represents the amount of deformation in rotor towards air gap. And the main deformation happens mainly in the x-axis direction. Therefore, U_{total} can be used in the following analysis.

Based on the model, Fig. 5.5 illustrates the rotor deformation distribution under the worst-case operating condition (25000 rpm and 180 °C). As observed, the maximum deformation consistently occurs at the center of the

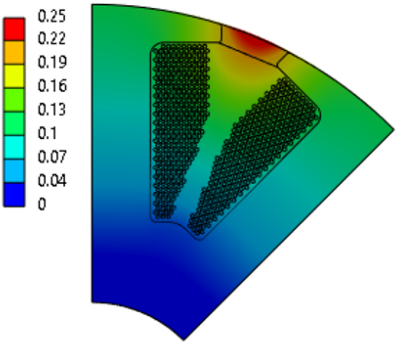

(a) Without sleeve.

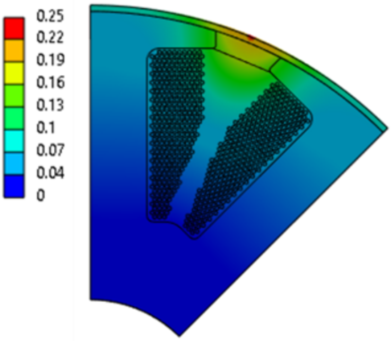

(b) Titanium alloy sleeve.

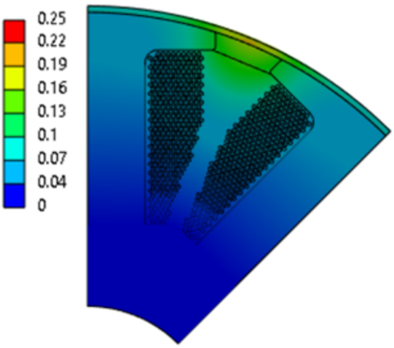

(c) Carbon fiber sleeve.

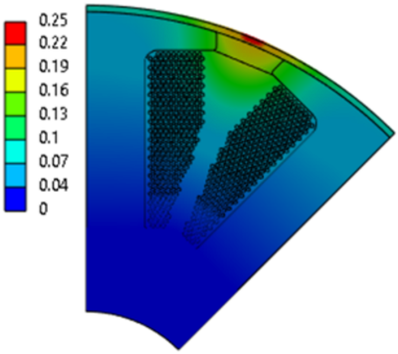

(d) Inconel 718 sleeve.

Figure 5.5: Comparison of rotor deformation distributions at 25000 rpm and 180 °C for different sleeve configurations: (a) without sleeve, (b) titanium alloy sleeve, (c) carbon-fiber sleeve, and (d) Inconel 718 sleeve.

wedge's outer surface. When a sleeve is applied, the maximum deformation shifts to the central region of the sleeve's outer surface, maintaining the same radial direction. Furthermore, the rotor without a sleeve has a larger maximum deformation compared to configurations with a sleeve. Among the three sleeve materials evaluated, the carbon fiber sleeve provides the most effective reduction in deformation.

5.4 Stress and Deformation Analysis

Based on the analytical and simulation studies conducted in Sections 5.2 and 5.3, this section investigates the stress and deformation behavior of the rotor–sleeve structure. The focus is on separating the effects caused by thermal expansion and centrifugal force, in order to better understand their individual contributions to the overall mechanical response.

5.4.1 Stress Analysis

The thermal expansion of the winding generates significant stress along all contact surfaces within the rotor slot. During rotation, the centrifugal force additionally increases stress on the same surfaces, particularly concentrated in the pole shoe region. Therefore, the analysis of stress focuses on the maximum equivalent stress observed at this location. In the simulation setup, the environment temperature is defined as 20 °C. Under this condition, thermal expansion is assumed to be negligible, and the stress is primarily attributed to centrifugal force. In addition, the stress calculated at 0 rpm is considered to result entirely from thermal expansion, as no centrifugal loading is present. These two operating conditions are used to decouple and evaluate the individual contributions of thermal and mechanical loading to the rotor's overall stress profile.

Fig. 5.6 presents the percentage of maximum stress at the pole shoe corner relative to the total stress under 60 °C. Fig. 5.7 shows the proportion of stress at the pole shoe corner attributed to thermal expansion, relative to the total stress at a constant speed of 25000 rpm under different temperature conditions.

As shown in Fig. 5.6 and Fig. 5.7, the stress contribution from centrifugal force increases with speed, while the stress contribution from thermal

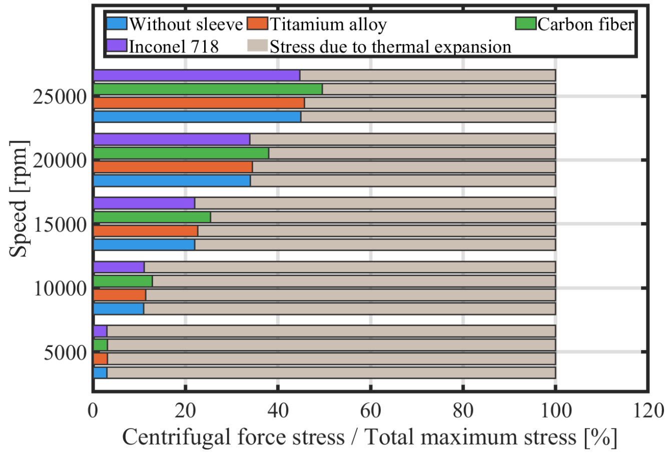

Figure 5.6: Percentage of maximum equivalent stress due to centrifugal force in pole shoe corners at 60 °C with varied speed.

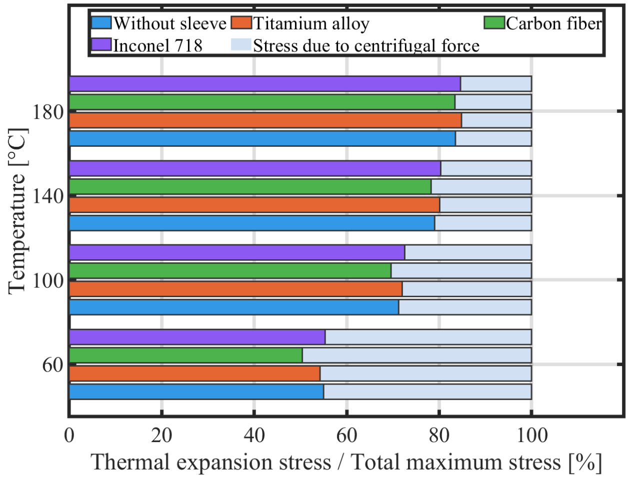

Figure 5.7: Percentage of maximum equivalent stress due to thermal expansion in pole shoe corners at 25000 rpm with varied temperature.

expansion increases with temperature. This trend remains consistent across rotors with different sleeve configurations. At lower temperatures and higher speeds, the stresses resulting from centrifugal force and thermal expansion are approximately equal. However, at higher temperatures, thermal expansion becomes the main contributor to rotor pole stress, regardless of the speed. Furthermore, the rotor with the carbon fiber sleeve exhibits the lowest stress contribution from thermal expansion. This is attributed to the low CTE of carbon fiber, which results in minimal thermal deformation compared to other sleeve materials under identical thermal conditions.

Fig. 5.8 illustrates the maximum rotor stress reduction achieved with different sleeve materials and operating conditions, relative to a rotor without a sleeve. As shown, all three sleeve materials reduce rotor stress by more than 30%, confirming the effectiveness of sleeve different conditions. Among the materials, the carbon fiber sleeve provides the most significant stress reduction, reaching up to 53.4% under the worst-case condition. All sleeves show a higher stress reduction percentage at 20 °C than at higher temperatures because thermal expansion is assumed to be negligible at 20 °C. At higher temperatures, sleeve expansion increases the mechanical load on rotor lamination, reducing the stress reduction effect.

To ensure compatibility with practical manufacturing processes, sleeve thicknesses ranging from 0.2 mm to 1 mm were considered. The maximum stress at the pole-shoe corner is assumed to arise exclusively from thermal expansion and centrifugal forces. Based on this assumption, the proportion of stress caused by thermal expansion is considered indicative of the relative contribution from centrifugal force. A higher percentage of stress attributed to thermal expansion indicates a correspondingly lower contribution from centrifugal force. Figure 5.9 illustrates the percentage of stress caused by thermal expansion for various sleeve materials across the selected thickness range, under worst operating conditions (180 °C and 25000 rpm). Fig. 5.10 presents the maximum stress in rotor with different sleeves under the worst case. The results indicate that this percentage remains relatively stable around 83%, regardless of sleeve material or thickness. This consistency suggests that thermal expansion is the main contributor to total stress under high-temperature conditions. In addition, carbon fiber provides better performance at high temperature compared with the other two sleeve materials.

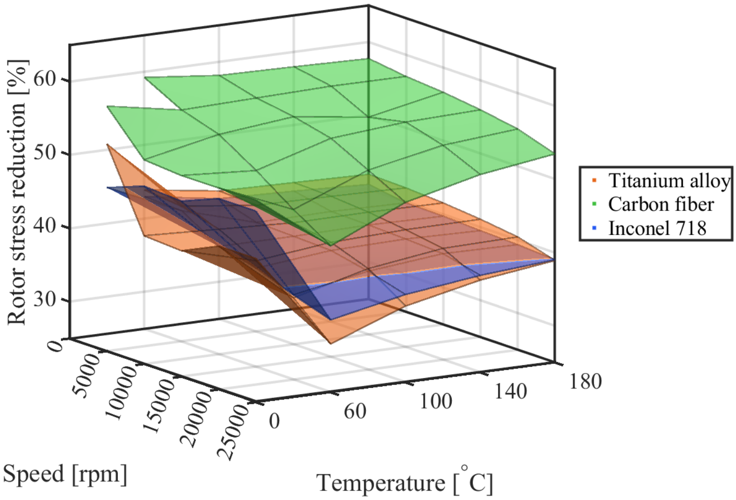

Figure 5.8: Rotor stress reduction percentage with different sleeve materials and varied conditions.

5.4.2 Deformation Analysis

Based on the same assumptions as in the stress analysis, rotor deformation is considered solely due to thermal expansion at zero rotational speed, and entirely due to centrifugal force at the temperature of 20 °C. The deformation in rotor resulting from centrifugal force and thermal expansion are analyzed separately in this section.

Figure 5.11 shows the percentage of maximum deformation caused by centrifugal force at a constant temperature of 60 °C, evaluated with varying rotational speeds. Figure 5.12 presents the properties of maximum deformation due to thermal expansion at a fixed speed of 25000 rpm, under different temperature conditions. From these figures, the rotor deformation due to centrifugal force increases with speed, while deformation caused by thermal expansion increases with temperature. Among the sleeve materials, the rotor with carbon fiber sleeve exhibits the lowest thermal deformation, attributed to low CTE. Despite this, thermal expansion remains the main source of total deformation across all operating conditions. Under high-speed and low-temperature conditions, it contributes more than 75% of the total deformation.

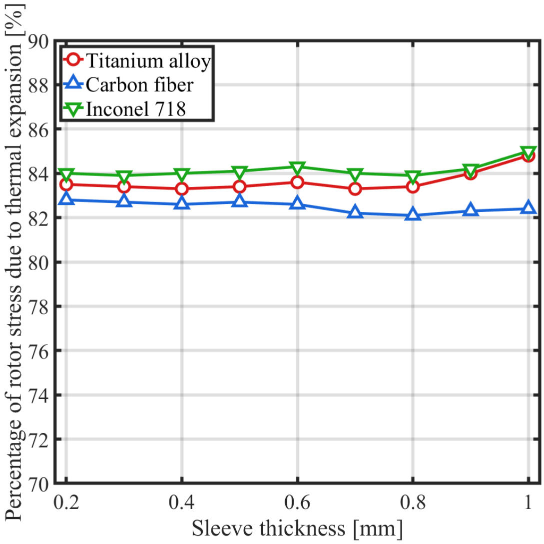

Figure 5.9: Percentage of maximum stress in pole shoe corners at 25000 rpm and 180 °C with varied sleeve thickness and sleeve materials.

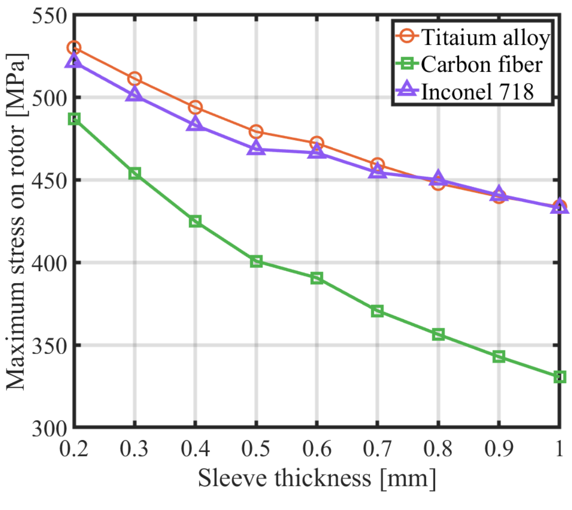

Figure 5.10: Maximum stress in pole shoe corners at 25000 rpm and 180 °C with varied sleeve thickness and sleeve materials.

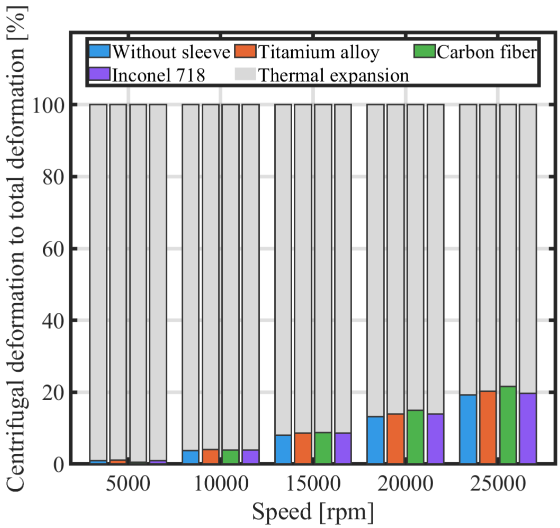

Figure 5.11: Percentage of maximum deformation due to centrifugal force at 60 °C with varied speed.

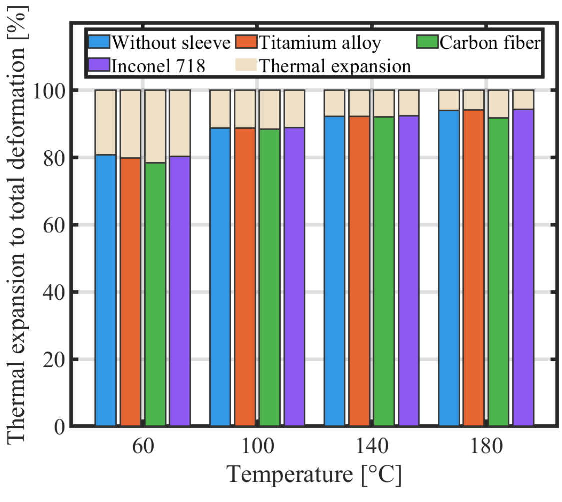

Figure 5.12: Percentage of maximum deformation due to thermal expansion at 25000 rpm with varied temperature.

Figure 5.13 shows the percentage of rotor deformation attributed to thermal expansion for three sleeve materials across varying thicknesses under the worst condition. For carbon fiber sleeves, this proportion decreases slightly with increasing thickness, whereas for titanium alloy and Overall, thermal expansion remains the primary cause of total deformation for all sleeve materials and thicknesses.

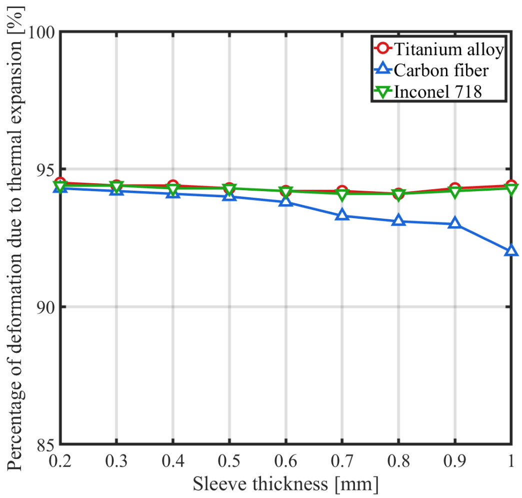

Figure 5.13: Percentage of maximum deformation in rotor at 25000 rpm and 180 °C with varied sleeve thickness and sleeve materials.

The impact of maximum deformation on the total air gap is also analyzed. Figure 5.14 illustrates the reduction of the air gap caused by deformation under the worst case operating condition for different sleeve materials and thicknesses. The percentage of air gap reduction in Figure 5.14 represents the portion of deformation relative to the total air gap length. In this paper, the machine air gap length is 1.5 mm. As shown, the air gap reduction decreases as the sleeve thickness increases for all three sleeve materials. Among the options, the carbon fiber sleeve demonstrates the lowest air gap reduction across all thicknesses, and the benefit in reduction becomes increasingly evident as the sleeve thickness increases. This is mainly due to the lower CTE of carbon fiber, which provides better dimensional stability at high temperature.

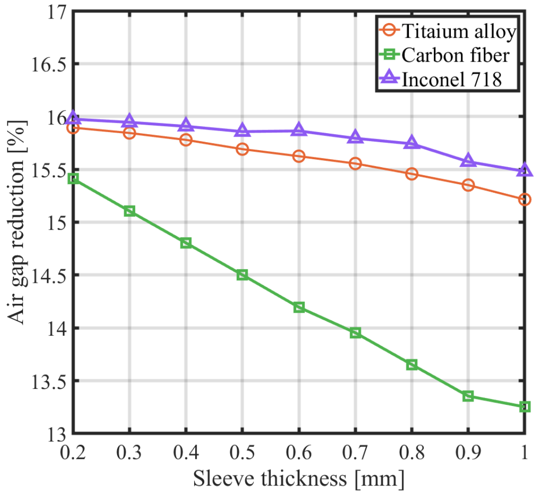

Figure 5.14: Machine air gap reduction due to deformation with different sleeve at 25000 rpm and 180 °C.

5.5 Application analysis

In this section, the EESM is evaluated in vehicle-oriented applications. To extend the analysis to broader use conditions, three representative operating conditions are considered in this subsection: a typical industrial condition, a traction drive condition, and the worst operating point. The typical industrial condition reflects low-speed, high-torque operation mainly found in pumps and fans., with 5000 rpm and 180 °C selected for this study. The traction condition represents normal vehicle operation and is analyzed at 10000 rpm and 150 °C. 25000 rpm and 180 °C are chosen for the worst-case analysis.

Figure 5.15 and Figure 5.16 present the maximum stress and maximum deformation under these operating conditions. The figures also illustrate the contributions from centrifugal force and thermal expansion separately. Compared with the other sleeve materials, carbon fiber provides the most effective overall performance in mechanical protection across all application conditions. Titanium alloy and Inconel 718 can also reduce the maximum rotor stress and deformation, although the effectiveness is comparatively limited.

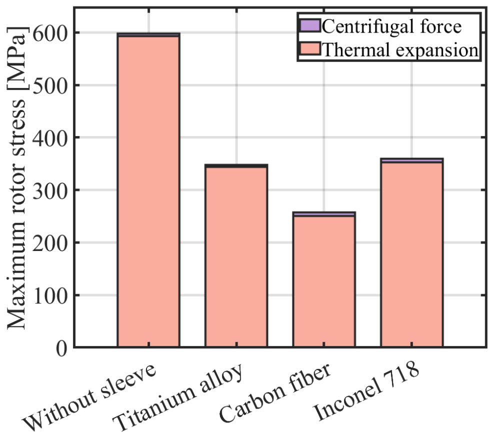

(a)

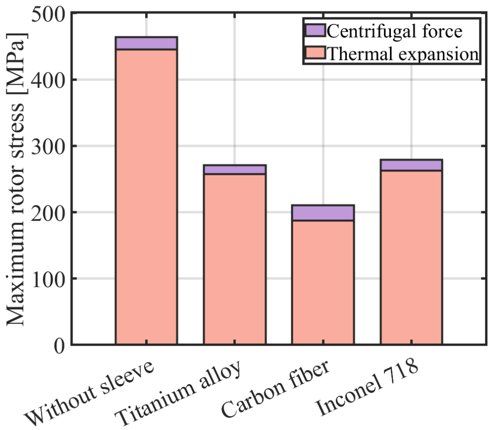

(b)

Figure 5.15: Maximum stress of rotor in different conditions: (a) typical industrial application, (b) traction application and (c)the worst condition.

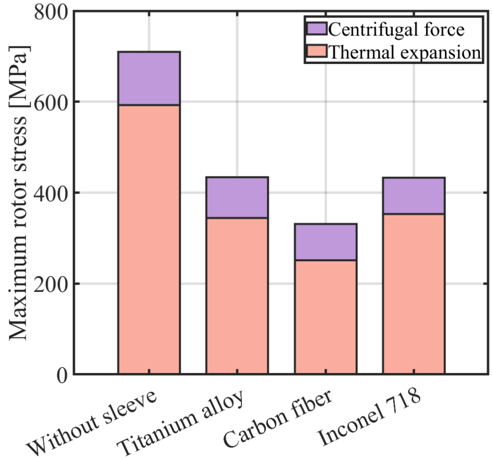

(c)

Figure 5.15: Maximum stress of rotor in different conditions: (a) typical industrial application, (b) traction application and (c)the worst condition.

For the typical industrial operating condition, the comparatively low rotational speed results in the smallest stress and deformation caused by centrifugal force among the three investigated cases. Consequently, the mechanical behavior of the rotor is primarily caused by thermal expansion, while the contribution of centrifugal force remains limited. As the operating condition shifts to traction applications, the higher rotor speed increases the influence of centrifugal force, leading to a increase in both stress and deformation. Nevertheless, thermal expansion continues to dominate the rotor response, contributing more than 90% of the total stress and deformation.

Under the worst case operating condition, which combines the highest rotational speed and temperature, the rotor experiences the maximum stress and deformation levels among the three cases. Although the contribution of centrifugal loading increases substantially with speed, thermal expansion remains the main source of mechanical loading in all investigated cases. These findings demonstrate that rotor temperature has a bigger influence on the mechanical stability of the investigated high-speed EESM than centrifugal force.

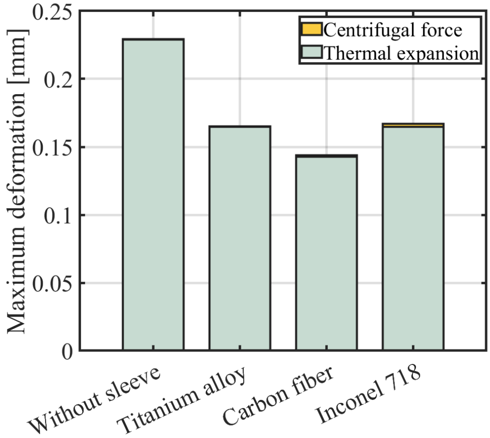

(a)

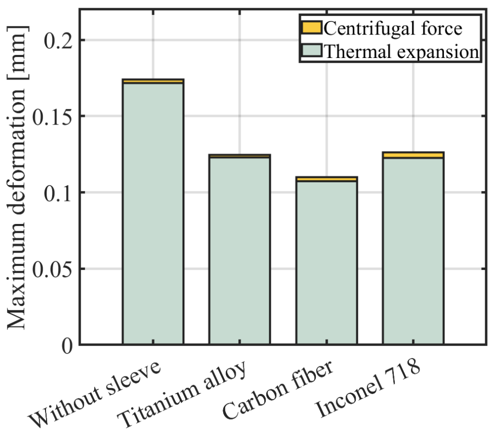

(b)

Figure 5.16: Maximum deformation of rotor in different conditions: (a) typical industrial application, (b) traction application and (c)the worst condition.

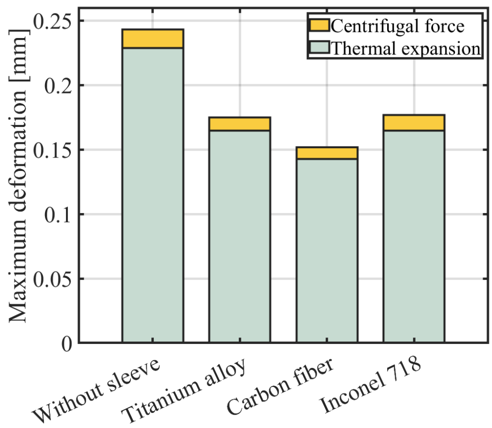

(c)

Figure 5.16: Maximum deformation of rotor in different conditions: (a) typical industrial application, (b) traction application and (c)the worst condition.

5.6 Mechanical analysis conclusion

In this chapter, the contributions of thermal expansion and centrifugal force to the maximum rotor stress and deformation in EESMs are analyzed separately. Thermal expansion effects increase with temperature, whereas centrifugal force contributions increase with speed. Thermal expansion has a more significant impact than centrifugal force on rotor stress and deformation, particularly at high temperatures. The highest percentage contribution from centrifugal force occurs under high-speed and low temperature conditions. At 25000 rpm and 60 °C, centrifugal force contributes 45.1% of the maximum stress and 18.9% of the deformation, both remaining lower than the respective contributions from thermal expansion.

For the analysis of rotors with the three sleeve materials, the overall trends are consistent. The carbon fiber sleeve leads the lowest stress and deformation caused by thermal expansion compared with the titanium-alloy and Inconel 718 sleeves. As the sleeve thickness increases, the maximum rotor stress and deformation decrease for all materials, with carbon fiber exhibiting the lowest stress and deformation values. Across the different application conditions analyzed, carbon fiber demonstrates the most effective performance for the EESM considered in this study. These results can provide useful guidance for the mechanical design of EESM rotor structures.

CHAPTER 6

Conclusion and future work

6.1 Conclusion

This thesis has presented a comprehensive investigation of the design and application of high-speed EESMs, with a particular focus on electromagnetic loss, operating conditions, and structural considerations. By using the WLTC driving cycle, the efficiency map reveals that the motor operates across a broad speed range, reflecting realistic and varying driving conditions. The operating points corresponding to highway, countryside, and urban scenarios are largely positioned within high-efficiency regions, typically above 96–97%, indicating that the machine performs near its optimal efficiency in most cases. Under highway driving conditions, the EESM achieves an efficiency of 97.31%, compared with 92.37% for the PMSM, indicating the better performance under high-speed operation. In terms of dynamic performance, the vehicle achieves a 0–100 km/h acceleration time of 8.1 s. This result is comparable to typical light electric vehicles, demonstrating competitive performance. The acceleration is adequate for light vehicle applications where efficiency, cost, and overall system optimization are prioritized. Through the development of a 2D model by FEM, the influence of stator current angle and rotor excitation on

AC losses in hairpin windings has been evaluated. The findings indicate that these parameters significantly modify the airgap flux distribution and flux leakage, thereby directly influencing the magnitude of AC losses. Such effects become increasingly critical under high-speed operating conditions, where loss components are amplified.

In addition, a 3D mechanical model of the rotor lamination has been established to assess structural performance at elevated rotational speeds. The analysis separately characterizes the effects of centrifugal forces and thermal expansion on rotor stress and deformation. The results demonstrate that thermal effects dominate the mechanical performance, especially at higher temperatures, leading to more pronounced stress and deformation compared to centrifugal loading. To enhance structural robustness, the application of external retaining sleeves has been explored. Among the candidate materials evaluated, carbon fiber exhibits superior performance by minimizing thermally induced stress and deformation.

Overall, this work provides insights into both the electromagnetic and mechanical design aspects of high-speed EESMs, offering practical guidance for improving efficiency, reliability, and structural stability in industrial applications.

6.2 Future work

The work presented in this thesis addresses key challenges associated with high-speed EESM, with particular emphasis on identifying suitable applications and optimizing both electromagnetic and mechanical design aspects.

Further, more specific suggestions for future work are:

- Investigating the impact of different hairpin materials on AC losses, with a comparative analysis of aluminum and copper hairpin windings under varying operating conditions.
- Explore additional frequency-related factors influencing AC losses in EESMs, with particular emphasis on high-speed operating conditions.
- Experimental evaluation of the overall efficiency and energy consumption of an EESM prototype across representative drive cycles.

References

[1] E. C. D.-G. for Climate Action, *Climate action progress report 2025 – strengthening competitiveness on the road to climate neutrality*, https://data.europa.eu/doi/10.2834/0963577, 2025.

[2] E. E. A. (EEA), *Monitoring of co2 emissions from vans, 2023*, https://www.eea.europa.eu/en/analysis/indicators/co2-performance-emissions-of-new, 2024.

[3] IEA, *Recycling of critical minerals*, https://www.iea.org/reports/recycling-of-critical-minerals, 2024.

[4] IEA, *Global critical minerals outlook 2025*, https://www.iea.org/reports/global-critical-minerals-outlook-2025, 2025.

[5] G. Fang, F. P. Scalcon, D. Xiao, R. P. Vieira, H. A. Gründling, and A. Emadi, "Advanced control of switched reluctance motors (srms): A review on current regulation, torque control and vibration suppression," *IEEE Open Journal of the Industrial Electronics Society*, vol. 2, pp. 280–301, 2021.

[6] F. P. Scalcon, G. Fang, C. J. V. Filho, H. A. Gründling, R. P. Vieira, and B. Nahid-Mobarakeh, "A review on switched reluctance generators in wind power applications: Fundamentals, control and future trends," *IEEE Access*, vol. 10, pp. 69 412–69 427, 2022.

[7] Z. Yang, F. Shang, I. P. Brown, and M. Krishnamurthy, "Comparative study of interior permanent magnet, induction, and switched reluctance

motor drives for ev and hev applications," *IEEE Transactions on Transportation Electrification*, vol. 1, no. 3, pp. 245–254, 2015.

[8] J. Cai, X. Dou, A. D. Cheok, W. Ding, Y. Yan, and X. Zhang, "Model predictive control strategies in switched reluctance motor drives—an overview," *IEEE Transactions on Power Electronics*, vol. 40, no. 1, pp. 1669–1685, 2025.

[9] G. Falekas, Z. Kolidakis, and A. Karlis, "Investigation of discrepancies between induction motor test results and design simulation," in *2024 International Conference on Electrical Machines (ICEM)*, 2024, pp. 1–7.

[10] T.-K. Kim et al., "Experimental comparison of induction motor and ipmsm with identical stator," in *2023 IEEE Energy Conversion Congress and Exposition (ECCE)*, 2023, pp. 4208–4215.

[11] T.-K. Kim et al., "Performance comparison of induction motors and ipmsms with identical stators for use as auxiliary motors in evs and hevs," *IEEE Transactions on Industry Applications*, vol. 62, no. 1, pp. 846–856, 2026.

[12] G. Mademlis, Y. Liu, J. Tang, L. Boscaglia, and N. Sharma, "Performance evaluation of electrically excited synchronous machine compared to pmsm for high-power traction drives," in *2020 International Conference on Electrical Machines (ICEM)*, vol. 1, 2020, pp. 1793–1799.

[13] S. Paul et al., "Feasibility study of electrically excited synchronous motor as electric vehicle traction motor," in *2025 28th International Conference on Electrical Machines and Systems (ICEMS)*, 2025, pp. 3584–3589.

[14] T. Xiao, Z. Ran, and Z.-Q. Zhu, "Comparison of electrically excited and synchronous reluctance machines with interior permanent magnet machines for evs/hevs," in *2023 26th International Conference on Electrical Machines and Systems (ICEMS)*, 2023, pp. 360–365.

[15] J. Mistry, M. H. Mohammadi, S. Sawardekar, and R. N. Zarandi, "Multiphysics design and optimization of high-speed traction motors," in *2025 IEEE Energy Conversion Conference Congress and Exposition (ECCE)*, 2025, pp. 1–8.

[16] A. Allahyari, I. Petrov, J. Pyrhönen, J. Montonen, and L. Aarniovuori, "Multiphysics design methodology for high-speed synchronous reluctance machines," *IEEE Transactions on Industry Applications*, pp. 1–12, 2025.

[17] K. Iwaki and K. Nakamura, "Design and prototype tests of magnetic-geared switched reluctance motor for in-wheel direct-drive evs," in *2024 International Conference on Electrical Machines (ICEM)*, 2024, pp. 1–6.

[18] J.-M. Ahn, D.-K. Lim, and M.-M. Koo, "Evolved motor design process to reduce the design expense of axial flux permanent magnet motor," *IEEE Access*, vol. 13, pp. 131 334–131 346, 2025.

[19] P. S. Ghahfarokhi, A. Podgornovs, A. J. M. Cardoso, A. Kallaste, A. Belahcen, and T. Vaimann, "Ac losses analysis approaches for electric vehicle motors with hairpin winding configuration," in *IECON 2021 – 47th Annual Conference of the IEEE Industrial Electronics Society*, 2021, pp. 1–4.

[20] S.-H. Park, J.-W. Chin, K.-S. Cha, J.-Y. Ryu, and M.-S. Lim, "Characteristic analysis of ipmsm for ev traction considering the effect of field and armature excitations on ac copper loss," in *2021 IEEE Energy Conversion Congress and Exposition (ECCE)*, 2021, pp. 4486–4491.

[21] Y. Liang, F. Zhao, K. Xu, W. Wang, J. Liu, and P. Yang, "Analysis of copper loss of permanent magnet synchronous motor with formed transposition winding," *IEEE Access*, vol. 9, pp. 101 105–101 114, 2021.

[22] T. Yu, Y. Gai, and J. Guo, "Ac copper loss analysis of hairpin windings for permanent magnet synchronous motors considering eddy current effects," in *2023 IEEE 6th Student Conference on Electric Machines and Systems (SCEMS)*, 2023, pp. 1–5.

[23] S. Xue, M. Michon, M. Popescu, and G. Volpe, "Optimisation of hairpin winding in electric traction motor applications," in *2021 IEEE International Electric Machines Drives Conference (IEMDC)*, 2021, pp. 1–7.

[24] Y. Wu, Z. Zhang, D. Chen, and S. Jin, "Investigation and comparison of different calculation methods for ac copper loss of flat copper wire in axial flux permanent magnet motor," *IEEE Transactions on Energy Conversion*, vol. 39, no. 1, pp. 169–181, 2024.

[25] H. Zhao et al., “Effectiveness of thermal interface materials on electrical machines thermal performance with heat pipes,” *IEEE Transactions on Transportation Electrification*, vol. 10, no. 1, pp. 1274–1285, 2024.

[26] S.-W. Hwang, J.-Y. Ryu, J.-W. Chin, S.-H. Park, D.-K. Kim, and M.-S. Lim, “Coupled electromagnetic-thermal analysis for predicting traction motor characteristics according to electric vehicle driving cycle,” *IEEE Transactions on Vehicular Technology*, vol. 70, no. 5, pp. 4262–4272, 2021.

[27] H. Barua, L. Lin, V. Rallabandi, J. Wilkins, P. Kumar, and B. Ozpineci, “Mechanical and vibration analysis of a high-speed outer rotor electric motor,” *IEEE Access*, vol. 12, pp. 137 881–137 892, 2024.

[28] E. A. Grunditz, “Design and assessment of battery electric vehicle powertrain, with respect to performance, energy consumption and electric motor thermal capability,” Ph.D. dissertation, Chalmers University of Technology, Gothenburg, 2016.

[29] E. A. Grunditz and A. Thiringer, “Performance analysis of current bevs based on a comprehensive review of specifications,” *IEEE Transactions on Transportation Electrification*, vol. 2, no. 3, pp. 270–289, Sep. 2016.